Available online at www.sciencedirect.com
SCIENCE DIRECT®
Comput. Methods Appl. Mech. Engrg. 195 (2006) 5962–5982
Computer methods in applied mechanics and engineering
www.elsevier.com/locate/cma

A mode decoupling continuum shape sensitivity method for fracture analysis of functionally graded materials

Sharif Rahman [a], B.N. Rao [b,*]

[a] Department of Mechanical Engineering, The University of Iowa, Iowa City, IA 52242, United States
[b] Structural Engineering Division, Department of Civil Engineering, Indian Institute of Technology, Madras, Chennai 600 036, India

Received 5 January 2005; received in revised form 22 June 2005; accepted 29 September 2005

Abstract

In this paper new mode decoupling continuum shape sensitivity method for calculating mixed-mode stress-intensity factors for a stationary crack in two-dimensional, linear-elastic, functionally graded materials with arbitrary geometry is presented. The proposed method involves the mode decoupling of deformations, the material derivative concept taken from continuum mechanics, and direct differentiation. The discrete form of the energy release rate is simple and easy to calculate, as it only requires multiplication of displacement vectors and stiffness sensitivity matrices. By judiciously selecting the velocity field, the method only requires displacement response in a sub domain close to the crack tip, thus making the method computationally efficient. Excellent agreement is obtained between stress-intensity factors predicted by the proposed method and available reference solutions in the literature. Therefore, mode decoupling shape sensitivity analysis provides an attractive alternative to fracture analysis of cracks in homogeneous and non-homogeneous materials.

Keywords: Crack; Functionally graded materials; Mode decoupling; Shape sensitivity analysis; Velocity field; Material derivative; Finite element method and stress-intensity factor

1. Introduction

Ever increasing multi-functional, structural performance demands in aerospace, transportation, energy, electronics, biomedical engineering, and other applications have spurred the development of a new class of materials called functionally graded materials (FGMs). FGMs engineered to meet a pre-determined functional performance [1,2] are multi-phase materials with volume fractions of the constituents varying gradually in a pre-determined profile, thus yielding a non-uniform microstructure in the material with continuously graded properties. Given the nature of processing techniques, graded materials can become anisotropic. For example, graded materials processed by a plasma spray technique generally have a lamellar structure [3], whereas processing by electron beam physical vapor deposition would lead to a highly columnar structure [4]. Such materials would not be isotropic, but orthotropic, with material directions that can be considered perpendicular to one another in an initial approximation. In recent years, various theoretical, computational, and experimental studies have been conducted to understand the fracture behavior of FGMs. A collection of technical papers, published in Volume 69, Issues 14–16 of [5] *Engineering Fracture Mechanics* (2002) reflects such state-of-the-art research into FGM fracture. A major component of such studies involves calculating crack-driving forces in FGMs accurately and efficiently.

* Corresponding author. Tel.: +91 44 22574285; fax: +91 44 22575286.
E-mail address: bnrao@iitm.ac.in (B.N. Rao).

0045-7825/$ - see front matter © 2005 Elsevier B.V. All rights reserved.
doi:10.1016/j.cma.2005.09.015

Consequently, various numerical methods have been developed or examined to calculate stress-intensity factors (SIFs), such as the displacement correlation method, the modified crack-closure integral method, the J_k^*-integral method and others [6]. More recently the interaction integral methods [7,8] that are simpler and more efficient have emerged as a useful and viable alternative to existing methods for mixed-mode fracture analysis of cracks in both isotropic and orthotropic FGMs. In contrast to existing methods, for the interaction integral methods it is not necessary to perform integration along the crack face of the discontinuity. Nevertheless, the majority of current numerical methods for FGM fracture analysis stem from extensions to methods originally developed for cracks in homogeneous materials.

An alternative approach to previously developed methods involves shape sensitivity analysis, which is frequently employed in structural design optimization. Shape sensitivity analysis permits direct, analytical evaluation of first-order (and higher-order, if required) derivatives of potential energy with respect to crack size. Broadly speaking, there are two fundamentally different approaches to shape sensitivity analysis. The first, known as the discrete approach, employs a discretized numerical model (e.g., finite element method [FEM], boundary element method [BEM], mesh-free method, etc.) to approximate the potential energy and then transforms shape derivatives into differentiations of algebraic equations by controlling node motions. For instance, Ishikawa [9] proposed a virtual crack extension method for mode separation of the energy release rate into mode I and mode II components and evaluated the mixed-mode SIFs. The second, known as the continuum approach and adopted in the present work, relies on the variational formulation used in continuum mechanics [10]. In this approach, shape sensitivity analysis is conducted by introducing a smooth velocity field to simulate shape change of the initial domain due to the crack advance. While discrete and continuum approaches are related (the former is an approximation of the latter), the continuum approach has two principal advantages: (1) a rigorous mathematical theory is obtained, without the uncertainty/errors associated with finite-dimensional approximation errors; and (2) explicit relations for sensitivity are obtained in terms of physical quantities rather than in terms of sums of derivatives of element matrices. These characteristic features of the continuum approach are of major importance in developing structural optimization theory [11,12].

For homogeneous materials, several shape sensitivity methods involving discrete [13–15] and continuum [16–19] formulations have appeared in calculating SIFs. Both FEM and BEM have been employed for the shape sensitivity analysis of cracks. Most of these investigations are applicable only to linear-elastic fracture-mechanics problems. More recently, continuum shape sensitivity methods have also been developed for predicting first-order sensitivities of mixed-mode SIFs for isotropic materials [20–22]. These analytical sensitivities of SIFs provide a convenient means by which subsequent fracture reliability analysis can be performed accurately and efficiently. However, all of the aforementioned shape sensitivity methods are strictly applicable to homogeneous materials. As a result, there is considerable interest in developing shape sensitivity methods for the numerical evaluation of crack-driving forces in FGM. With this need in mind, the authors recently developed a continuum shape sensitivity methods for calculating mixed-mode SIFs for a stationary crack in two-dimensional, linear-elastic, isotropic and orthotropic FGMs of arbitrary geometry [23,24]. However, these methods involve superposition of mode I or mode II near crack tip displacement and stress fields on the *actual* state for given boundary conditions.

This paper presents a mode decoupling continuum shape sensitivity method for calculating mixed-mode SIFs for a stationary crack in two-dimensional, linear-elastic, FGMs of arbitrary geometry. The method involves the mode decoupling of deformations, the material derivative concept taken from continuum mechanics, and direct differentiation. Since the governing variational equation is differentiated prior to discretization, resulting sensitivity equations are independent of approximate numerical techniques, such as FEM, BEM, the mesh-free method, or others. Six numerical examples involving both isotropic and orthotropic FGMs, in conjunction with FEM are presented to evaluate the accuracy of fracture parameters calculated by the proposed method. Comparisons have been made between the SIFs predicted by the proposed method and available reference solutions in the literature, generated either analytically or numerically using various other fracture integrals or analyses.

2. Shape sensitivity analysis

2.1. Velocity field

Consider a general three-dimensional body with a specific configuration, referred to as the initial (reference) configuration, with domain Ω, boundary Γ, and a body material point identified by position vector $\boldsymbol{x} \in \Omega$. Consider the body's motion from an initial configuration with domain Ω and boundary Γ into a perturbed configuration with domain Ω_τ and boundary Γ_τ, as shown in Fig. 1. This process can be expressed as

$$\boldsymbol{T} : \boldsymbol{x} \to \boldsymbol{x}_\tau, \quad \boldsymbol{x} \in \Omega, \tag{1}$$

where $\boldsymbol{x}_\tau$ is the position vector of the material point in the perturbed configuration, $\boldsymbol{T}$ is a transformation mapping, and $\tau \in \mathbb{R}^+$ is a scalar, fictitious, time-like parameter denoting the amount of shape change, with

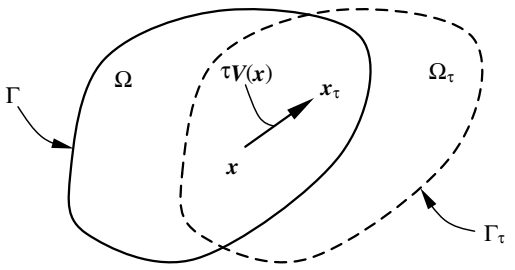

Fig. 1. Variation of domain.

$$\begin{aligned} \boldsymbol{x}_\tau &= \boldsymbol{T}(\boldsymbol{x},\tau), \\ \Omega_\tau &= \boldsymbol{T}(\Omega,\tau), \\ \Gamma_\tau &= \boldsymbol{T}(\Gamma,\tau). \end{aligned} \tag{2}$$

A velocity field can then be defined as

$$\boldsymbol{v}(\boldsymbol{x}_\tau,\tau) \equiv \frac{\mathrm{d}\boldsymbol{x}_\tau}{\mathrm{d}\tau} = \frac{\mathrm{d}\boldsymbol{T}(\boldsymbol{x},\tau)}{\mathrm{d}\tau} = \frac{\partial \boldsymbol{T}(\boldsymbol{x},\tau)}{\partial\tau}. \tag{3}$$

In the neighborhood of the initial time $\tau = 0$, assuming a regularity hypothesis and ignoring high-order terms,

$$\boldsymbol{x}_\tau = \boldsymbol{T}(\boldsymbol{x},\tau) = \boldsymbol{T}(\boldsymbol{x},0) + \tau\frac{\partial \boldsymbol{T}(\boldsymbol{x},0)}{\partial\tau} + \mathrm{O}(\tau^2) \cong \boldsymbol{x} + \tau\boldsymbol{v}(\boldsymbol{x},0), \tag{4}$$

where $\boldsymbol{x} = \boldsymbol{T}(\boldsymbol{x}, 0)$. For the rest of this paper, the velocity field $\boldsymbol{v}(\boldsymbol{x}, 0)$ will be denoted by $\boldsymbol{V}(\boldsymbol{x})$ or $\boldsymbol{V}$. Thus, a velocity field characterizes the direction of domain variation, which implies that for a given $\boldsymbol{V}(\boldsymbol{x})$, the shape change of Ω is uniquely controlled by the scalar parameter τ.

2.2. Sensitivity analysis

The variational governing equation for a linear-elastic, non-homogeneous or homogeneous solid with domain Ω can be formulated as [12]

$$a_\Omega(\boldsymbol{z},\bar{\boldsymbol{z}}) = \ell_\Omega(\bar{\boldsymbol{z}}), \quad \text{for all } \bar{\boldsymbol{z}} \in \boldsymbol{Z}, \tag{5}$$

where $\boldsymbol{z}$ and $\bar{\boldsymbol{z}}$ are the actual and virtual displacement fields of the structure, respectively, $\boldsymbol{Z}$ is the space of kinematically admissible virtual displacements, and $a_\Omega(\boldsymbol{z},\bar{\boldsymbol{z}})$ and $\ell_\Omega(\bar{\boldsymbol{z}})$ are energy bilinear and load linear forms, respectively. The subscript Ω in Eq. (5) is used to indicate the dependency of the governing equation on the shape of the structural domain. If $\boldsymbol{z}_\tau(\boldsymbol{x}_\tau)$ represents the displacement at $\boldsymbol{x}_\tau = \boldsymbol{x} + \tau\boldsymbol{V}(\boldsymbol{x})$ of the perturbed domain, the point-wise material derivative at $\boldsymbol{x} \in \Omega$ is defined as [12]

$$\dot{\boldsymbol{z}}(\boldsymbol{x}) \equiv \lim_{\tau\to 0}\left[\frac{\boldsymbol{z}_\tau(\boldsymbol{x}+\tau\boldsymbol{V}(\boldsymbol{x})) - \boldsymbol{z}(\boldsymbol{x})}{\tau}\right] = \boldsymbol{z}'(\boldsymbol{x}) + \nabla\boldsymbol{z}^{\mathrm{T}}\boldsymbol{V}(\boldsymbol{x}), \tag{6}$$

where

$$\boldsymbol{z}' = \lim_{\tau\to 0}\left[\frac{\boldsymbol{z}_\tau(\boldsymbol{x}) - \boldsymbol{z}(\boldsymbol{x})}{\tau}\right] \tag{7}$$

is the partial derivative of $\boldsymbol{z}$ and $\nabla = \{\partial/\partial x_1, \partial/\partial x_2, \partial/\partial x_3\}^{\mathrm{T}}$ is the vector of gradient operators.

If no body forces are involved, the variational equation (Eq. (5)) can be written as

$$a_\Omega(\boldsymbol{z},\bar{\boldsymbol{z}}) \equiv \int_\Omega \sigma_{ij}(\boldsymbol{z})\varepsilon_{ij}(\bar{\boldsymbol{z}})\,\mathrm{d}\Omega = \ell_\Omega(\bar{\boldsymbol{z}}) \equiv \int_\Gamma T_i\bar{z}_i\,\mathrm{d}\Gamma, \tag{8}$$

where $\sigma_{ij}(\boldsymbol{z})$ and $\varepsilon_{ij}(\bar{\boldsymbol{z}})$ are components of the stress and strain tensors of the displacement $\boldsymbol{z}$ and virtual displacement $\bar{\boldsymbol{z}}$, respectively, T_i is the ith component of the surface traction, and $\bar{z}_i$ is the ith component of $\bar{\boldsymbol{z}}$. Taking the material derivative of both sides of Eq. (8), it can be shown that [12]

$$a_\Omega(\dot{\boldsymbol{z}},\bar{\boldsymbol{z}}) = \ell'_{\boldsymbol{V}}(\bar{\boldsymbol{z}}) - a'_{\boldsymbol{V}}(\boldsymbol{z},\bar{\boldsymbol{z}}), \quad \forall\bar{\boldsymbol{z}} \in \boldsymbol{Z}, \tag{9}$$

where the subscript $\boldsymbol{V}$ indicates the dependency of the terms on the velocity field. The terms $\ell'_{\boldsymbol{V}}(\bar{\boldsymbol{z}})$ and $a'_{\boldsymbol{V}}(\boldsymbol{z},\bar{\boldsymbol{z}})$ can be further derived as [12]

$$\ell'_{\boldsymbol{V}}(\bar{\boldsymbol{z}}) = \int_{\Gamma} \left\{ -T_i(\bar{z}_{i,j}V_j) + [(T_i\bar{z}_i)_{,j}n_j + \kappa_\Gamma(T_i\bar{z}_i)](V_i n_i) \right\} \mathrm{d}\Gamma \tag{10}$$

and

$$a'_{\boldsymbol{V}}(\boldsymbol{z},\bar{\boldsymbol{z}}) = -\int_{\Omega} \left[\varepsilon_{ij}(\boldsymbol{z})D_{ijkl}(\boldsymbol{x})(\bar{z}_{k,m}V_{m,l}) + \varepsilon_{ij}(\bar{\boldsymbol{z}})D_{ijkl}(\boldsymbol{x})(z_{k,m}V_{m,l}) - \varepsilon_{ij}(\bar{\boldsymbol{z}})D_{ijkl,m}(\boldsymbol{x})\varepsilon_{kl}(\boldsymbol{z})V_m - \varepsilon_{ij}(\boldsymbol{z})D_{ijkl}(\boldsymbol{x})\varepsilon_{kl}(\bar{\boldsymbol{z}})\mathrm{div}\boldsymbol{V} \right] \mathrm{d}\Omega, \tag{11}$$

where n_i is the ith component of unit normal vector $\boldsymbol{n}$, κ_Γ is the curvature of the boundary, $z_{i,j} = \partial z_i/\partial x_j$, $\bar{z}_{i,j} = \partial \bar{z}_i/\partial x_j$, $V_{i,j} = \partial V_i/\partial x_j$, $D_{ijkl}(\boldsymbol{x})$ is a component of the constitutive tensor and $D_{ijkl,m}(\boldsymbol{x}) = \partial D_{ijkl}(\boldsymbol{x})/\partial x_m$. If the modulus of elasticity $E(\boldsymbol{x})$ is the only material property that varies, then $D_{ijkl,m}(\boldsymbol{x}) = [\partial E(\boldsymbol{x})/\partial x_m]D_{ijkl}(\boldsymbol{x})/E(\boldsymbol{x})$. Note that the third term in the integrand on the right hand side of Eq. (11) arises naturally in the formulation of a continuum shape sensitivity analysis for non-homogeneous materials, but vanishes for homogeneous materials. In addition, D_{ijkl} is constant for homogeneous materials.

3. Shape sensitivity method for fracture analysis

The method of mode decoupling/separation of deformations is an effective tool for calculating mixed-mode fracture parameters in homogeneous materials [9]. In this section, the method of mode decoupling of deformations is derived in conjunction with continuum shape sensitivity analysis to solve mixed-mode problems in isotropic and orthotropic FGMs. The study of FGM fracture analysis would enhance the understanding of a fracture in a generic material, since upon shrinking the gradient layer in FGM is expected to behave like a sharp interface, and upon expansion, the fracture behavior would be analogous to that of a homogeneous material.

3.1. Mode decoupling method for J-integral

Consider an arbitrary, two-dimensional cracked body of crack length a, with unit thickness subjected to an arbitrary loading as shown in Fig. 2. The total potential energy Π of the system, in the absence of body forces, is

$$\Pi \equiv \frac{1}{2}\int_{\Omega} \varepsilon_{ij}(\boldsymbol{z})D_{ijkl}\varepsilon_{kl}(\boldsymbol{z})\,\mathrm{d}\Omega - \int_{\Gamma} T_i z_i\,\mathrm{d}\Gamma. \tag{12}$$

Substituting $\bar{\boldsymbol{z}}$ with $\boldsymbol{z}$ in Eq. (8) and using Eq. (12) produce the following

$$\Pi = -\frac{1}{2}a_\Omega(\boldsymbol{z},\boldsymbol{z}). \tag{13}$$

The energy release rate is equal to the derivative of potential energy with respect to the crack area. For a two-dimensional cracked structure with unit thickness, the crack area is equal to crack length a. Assuming crack length a to be the variable of interest, a change in crack area or crack length involves a change in the shape of the cracked continuum. In relation to shape sensitivity theory, this change implies that the energy release rate is equal to the material derivative of potential

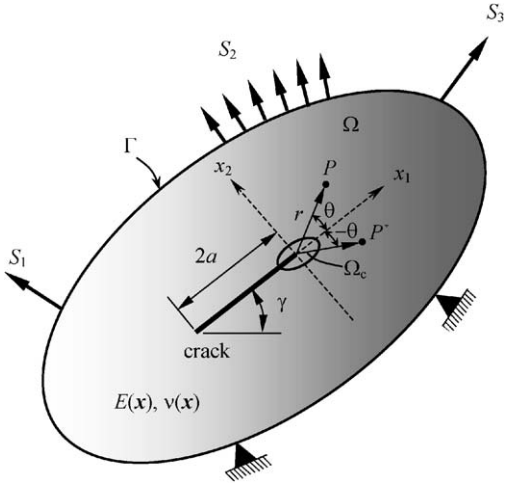

Fig. 2. A crack in a functionally graded material.

energy. Hence, for elastic (linear or nonlinear) solids under mixed-mode loading conditions, the J-integral, which is equal to the energy release rate, can be derived as

$$J \equiv -\dot{\Pi} = \frac{1}{2}[a_\Omega(\dot{\boldsymbol{z}}, \boldsymbol{z}) + a_\Omega(\boldsymbol{z}, \dot{\boldsymbol{z}}) + a'_{\boldsymbol{V}}(\boldsymbol{z}, \boldsymbol{z})], \tag{14}$$

where the over dot indicates a material derivative. If (1) velocity field $\boldsymbol{V}(\boldsymbol{x})$ is defined such that traction-loading boundary Γ is fixed, i.e., $\boldsymbol{V}(\boldsymbol{x}) = \boldsymbol{0}$ on the traction-loading boundary Γ, and (2) $\bar{\boldsymbol{z}}$ is replaced with $\boldsymbol{z}$ in Eq. (9), noting that $a_\Omega(\dot{\boldsymbol{z}}, \boldsymbol{z}) = a_\Omega(\boldsymbol{z}, \dot{\boldsymbol{z}}) = -a'_{\boldsymbol{V}}(\boldsymbol{z}, \boldsymbol{z})$, then

$$J = -\frac{1}{2}a'_{\boldsymbol{V}}(\boldsymbol{z}, \boldsymbol{z}). \tag{15}$$

Substituting the expression of $a'_{\boldsymbol{V}}(\boldsymbol{z}, \boldsymbol{z})$ from Eq. (11) and noting that D_{ijkl} is constant for homogeneous orthotropic materials ($D_{ijkl,m} = 0$) gives

$$J = \frac{1}{2}\int_\Omega [\sigma_{ij}(\boldsymbol{z})(z_{i,k}V_{k,j}) + \sigma_{ij}(\boldsymbol{z})(z_{i,k}V_{k,j}) - \sigma_{ij}(\boldsymbol{z})\varepsilon_{ij}(z)\mathrm{div}\,\boldsymbol{V}]\,\mathrm{d}\Omega. \tag{16}$$

By defining $W = \sigma_{ij}\varepsilon_{ij}/2$ as the strain energy density and $\boldsymbol{V}(\boldsymbol{x}) = \{V_1(\boldsymbol{x}), 0\}^{\mathrm{T}}$ as the velocity field, with $V_1(\boldsymbol{x})$ having a value of *unity* at the crack tip, *zero* along the boundary of the domain, and arbitrary elsewhere, the following equation is produced

$$J = \int_\Omega \left(\sigma_{ij}\frac{\partial z_i}{\partial x_1} - W\delta_{1j}\right)\frac{\partial V_1}{\partial x_j}\mathrm{d}\Omega, \tag{17}$$

which is the same as the traditional domain form of the J-integral, with V_1 taking the place of *weight function* q. Hence, weight function q can be considered the virtual change in crack length, having a value of *unity* at the crack tip, *zero* along the boundary of the domain, and arbitrary elsewhere.

For decoupling the J-Integral into mode I and mode II components, consider two points $P(x_1, x_2)$ and $P^*(x_1, -x_2)$ symmetric about the crack line (x_1-axis) as shown in Fig. 2. The stress, strain, displacement and traction fields can be separated analytically into mode I and mode II components within a symmetric region with respect to x_1-axis, in the neighborhood of the crack tip. Let the displacement, strain, and stress field parameters at point $P(x_1, x_2)$ be $\boldsymbol{z}$, $\varepsilon(\boldsymbol{z})$, $\sigma(\boldsymbol{z})$ respectively and at point $P^*(x_1, -x_2)$ be $\boldsymbol{z}^*$, $\varepsilon^*(\boldsymbol{z})$, $\sigma^*(\boldsymbol{z})$ respectively. Deformation of mode I and mode II are symmetric and skew symmetric, respectively, with respect to x_1-axis. First, let us consider the separation of displacement $\boldsymbol{z} = (z_1, z_2)$ into two components $\boldsymbol{z}^{\mathrm{I}} = (z_1^{\mathrm{I}}, z_2^{\mathrm{I}})$ and $\boldsymbol{z}^{\mathrm{II}} = (z_1^{\mathrm{II}}, z_2^{\mathrm{II}})$ of mode I and mode II. Because of the symmetrical deformation of mode I and skew symmetrical deformation of mode II with respect to the x_1-axis, $\boldsymbol{z}^{\mathrm{I}} = (z_1^{\mathrm{I}}, z_2^{\mathrm{I}})$ and $\boldsymbol{z}^{\mathrm{II}} = (z_1^{\mathrm{II}}, z_2^{\mathrm{II}})$ can also be defined

$$\boldsymbol{z} = \boldsymbol{z}^{\mathrm{I}} + \boldsymbol{z}^{\mathrm{II}}, \tag{18}$$

where

$$\begin{Bmatrix} z_1^{\mathrm{I}} \\ z_2^{\mathrm{I}} \end{Bmatrix} = \frac{1}{2}\begin{Bmatrix} z_1 + z_1^* \\ z_2 - z_2^* \end{Bmatrix} \tag{19}$$

and

$$\begin{Bmatrix} z_1^{\mathrm{II}} \\ z_2^{\mathrm{II}} \end{Bmatrix} = \frac{1}{2}\begin{Bmatrix} z_1 - z_1^* \\ z_2 + z_2^* \end{Bmatrix}. \tag{20}$$

Here, $()^*$ denotes the value of displacement, strain, stress, etc. at point P^* that is symmetrical point of point P with respect to the x_1-axis. For instance,

$$z_i^*(x_1, x_2) = z_i(x_1, -x_2). \tag{21}$$

Using these displacement components, z_i^{I} and z_i^{II}, strain components, $\varepsilon_{ij}^{\mathrm{I}}(\boldsymbol{z})$ related to z_i^{I} and $\varepsilon_{ij}^{\mathrm{II}}(\boldsymbol{z})$ related to z_i^{II}, are defined by a strain–displacement relation as follows:

$$\varepsilon_{ij}(\boldsymbol{z}) = (z_{i,j}^M + z_{j,i}^M)/2 \quad (M = \mathrm{I}, \mathrm{II}). \tag{22}$$

Substituting Eq. (18) into Eq. (22), we obtain

$$\varepsilon_{ij}(\boldsymbol{z}) = \varepsilon_{ij}^{\mathrm{I}}(\boldsymbol{z}) + \varepsilon_{ij}^{\mathrm{II}}(\boldsymbol{z}), \tag{23}$$

where

$$\begin{Bmatrix} \varepsilon^{\mathrm{I}}_{11}(z) \\ \varepsilon^{\mathrm{I}}_{22}(z) \\ \varepsilon^{\mathrm{I}}_{12}(z) \end{Bmatrix} = \frac{1}{2} \begin{Bmatrix} \varepsilon_{11}(z) + \varepsilon_{11}(z^*) \\ \varepsilon_{22}(z) + \varepsilon_{22}(z^*) \\ \varepsilon_{12}(z) - \varepsilon_{12}(z^*) \end{Bmatrix} \tag{24}$$

and

$$\begin{Bmatrix} \varepsilon^{\mathrm{II}}_{11}(z) \\ \varepsilon^{\mathrm{II}}_{22}(z) \\ \varepsilon^{\mathrm{II}}_{12}(z) \end{Bmatrix} = \frac{1}{2} \begin{Bmatrix} \varepsilon_{11}(z) - \varepsilon_{11}(z^*) \\ \varepsilon_{22}(z) - \varepsilon_{22}(z^*) \\ \varepsilon_{12}(z) + \varepsilon_{12}(z^*) \end{Bmatrix}. \tag{25}$$

Similarly, the stress components $\sigma_{ij}(z)$ at the point P can be separated in such a form the $\sigma_{ij}(z)$ is the sum of $\sigma^{\mathrm{I}}_{ij}(z)$ and $\sigma^{\mathrm{II}}_{ij}(z)$ that are expressed in terms of stress components $\sigma_{ij}(z)$ at point P of coordinates (x_1, x_2) and stress $\sigma_{ij}(z^*)$ at point P^* of coordinates $(x_1, -x_2)$ as shown below

$$\sigma_{ij}(z) = \sigma^{\mathrm{I}}_{ij}(z) + \sigma^{\mathrm{II}}_{ij}(z), \tag{26}$$

where

$$\begin{Bmatrix} \sigma^{\mathrm{I}}_{11}(z) \\ \sigma^{\mathrm{I}}_{22}(z) \\ \sigma^{\mathrm{I}}_{12}(z) \end{Bmatrix} = \frac{1}{2} \begin{Bmatrix} \sigma_{11}(z) + \sigma_{11}(z^*) \\ \sigma_{22}(z) + \sigma_{22}(z^*) \\ \sigma_{12}(z) - \sigma_{12}(z^*) \end{Bmatrix} \tag{27}$$

and

$$\begin{Bmatrix} \sigma^{\mathrm{II}}_{11}(z) \\ \sigma^{\mathrm{II}}_{22}(z) \\ \sigma^{\mathrm{II}}_{12}(z) \end{Bmatrix} = \frac{1}{2} \begin{Bmatrix} \sigma_{11}(z) - \sigma_{11}(z^*) \\ \sigma_{22}(z) - \sigma_{22}(z^*) \\ \sigma_{12}(z) + \sigma_{12}(z^*) \end{Bmatrix}. \tag{28}$$

By partially differentiating $\sigma_{ij}(z^*)$ with respect to x_2, we obtain

$$[\partial\sigma_{ij}(z^*)/\partial x_2]_{(x_1,x_2)} = -[\partial\sigma_{ij}(z)/\partial x_2]_{(x_1,-x_2)}. \tag{29}$$

Hence it can be shown that

$$\sigma^M_{ij,j}(z) = 0 \quad (M = \mathrm{I}, \mathrm{II}) \tag{30}$$

and

$$\sigma^M_{ij}(z) = \sigma^M_{ji}(z) \quad (M = \mathrm{I}, \mathrm{II}). \tag{31}$$

In other words, $\sigma^M_{ij}(z)$ $(M = \mathrm{I}, \mathrm{II})$ satisfy the equilibrium equation of force and that of moment. Substituting the relationships in Eqs. (18), (23) and (26) into Eq. (11) we obtain

$$\begin{aligned} J = {} & \frac{1}{2}\int_\Omega [\sigma^{\mathrm{I}}_{ij}(z)(z^{\mathrm{I}}_{i,k}V_{k,j}) + \sigma^{\mathrm{I}}_{ij}(z)(z^{\mathrm{I}}_{i,k}V_{k,j}) - \varepsilon^{\mathrm{I}}_{ij}(z)D_{ijkl,m}(x)\varepsilon^{\mathrm{I}}_{kl}(z)V_m - \sigma^{\mathrm{I}}_{ij}(z)\varepsilon^{\mathrm{I}}_{ij}(z)\mathrm{div}\, V]\mathrm{d}\Omega \\ & + \frac{1}{2}\int_\Omega [\sigma^{\mathrm{I}}_{ij}(z)(z^{\mathrm{II}}_{i,k}V_{k,j}) + \sigma^{\mathrm{I}}_{ij}(z)(z^{\mathrm{II}}_{i,k}V_{k,j}) - \varepsilon^{\mathrm{I}}_{ij}(z)D_{ijkl,m}(x)\varepsilon^{\mathrm{II}}_{kl}(z)V_m - \sigma^{\mathrm{I}}_{ij}(z)\varepsilon^{\mathrm{II}}_{ij}(z)\mathrm{div}\, V]\mathrm{d}\Omega \\ & + \frac{1}{2}\int_\Omega [\sigma^{\mathrm{II}}_{ij}(z)(z^{1}_{i,k}V_{k,j}) + \sigma^{\mathrm{II}}_{ij}(z)(z^{1}_{i,k}V_{k,j}) - \varepsilon^{\mathrm{II}}_{ij}(z)D_{ijkl,m}(x)\varepsilon^{\mathrm{I}}_{kl}(z)V_m - \sigma^{\mathrm{II}}_{ij}(z)\varepsilon^{\mathrm{I}}_{ij}(z)\mathrm{div}\, V]\mathrm{d}\Omega \\ & + \frac{1}{2}\int_\Omega [\sigma^{\mathrm{II}}_{ij}(z)(z^{\mathrm{II}}_{i,k}V_{k,j}) + \sigma^{\mathrm{II}}_{ij}(z)(z^{\mathrm{II}}_{i,k}V_{k,j}) - \varepsilon^{\mathrm{II}}_{ij}(z)D_{ijkl,m}(x)\varepsilon^{\mathrm{II}}_{kl}(z)V_m - \sigma^{\mathrm{II}}_{ij}(z)\varepsilon^{\mathrm{II}}_{ij}(z)\mathrm{div}\, V]\mathrm{d}\Omega. \end{aligned} \tag{32}$$

Since $[\partial(\,)/\partial x_2]_{(x_1,x_2)} = -[\partial(\,)/\partial x_2]_{(x_1,-x_2)}$, the second and third integrands in Eq. (32) reduce to zero, when evaluated in a symmetric region with respect to x_1-axis. Hence,

$$\begin{aligned} J = {} & \frac{1}{2}\int_\Omega [\sigma^{\mathrm{I}}_{ij}(z)(z^{\mathrm{I}}_{i,k}V_{k,j}) + \sigma^{\mathrm{I}}_{ij}(z)(z^{\mathrm{I}}_{i,k}V_{k,j}) - \varepsilon^{\mathrm{I}}_{ij}(z)D_{ijkl,m}(x)\varepsilon^{\mathrm{I}}_{kl}(z)V_m - \sigma^{\mathrm{I}}_{ij}(z)\varepsilon^{\mathrm{I}}_{ij}(z)\mathrm{div}\, V]\mathrm{d}\Omega \\ & + \frac{1}{2}\int_\Omega [\sigma^{\mathrm{II}}_{ij}(z)(z^{\mathrm{II}}_{i,k}V_{k,j}) + \sigma^{\mathrm{II}}_{ij}(z)(z^{\mathrm{II}}_{i,k}V_{k,j}) - \varepsilon^{\mathrm{II}}_{ij}(z)D_{ijkl,m}(x)\varepsilon^{\mathrm{II}}_{kl}(z)V_m - \sigma^{\mathrm{II}}_{ij}(z)\varepsilon^{\mathrm{II}}_{ij}(z)\mathrm{div}\, V]\mathrm{d}\Omega \cong J^{\mathrm{I}} + J^{\mathrm{II}}. \end{aligned} \tag{33}$$

Therefore using the above relationship the J-Integral can be decoupled into mode I and mode II components J^{I} and J^{II} as follows:

$$J^{\mathrm{I}} = \frac{1}{2}\int_{\Omega}[\sigma^{\mathrm{I}}_{ij}(\boldsymbol{z})(z^{\mathrm{I}}_{i,k}V_{k,j}) + \sigma^{\mathrm{I}}_{ij}(\boldsymbol{z})(z^{\mathrm{I}}_{i,k}V_{k,j}) - \varepsilon^{\mathrm{I}}_{ij}(\boldsymbol{z})D_{ijkl,m}(\boldsymbol{x})\varepsilon^{\mathrm{I}}_{kl}(\boldsymbol{z})V_m - \sigma^{\mathrm{I}}_{ij}(\boldsymbol{z})\varepsilon^{\mathrm{I}}_{ij}(\boldsymbol{z})\mathrm{div}\,\boldsymbol{V}]\mathrm{d}\Omega \tag{34}$$

and

$$J^{\mathrm{II}} = \frac{1}{2}\int_{\Omega}[\sigma^{\mathrm{II}}_{ij}(\boldsymbol{z})(z^{\mathrm{II}}_{i,k}V_{k,j}) + \sigma^{\mathrm{II}}_{ij}(\boldsymbol{z})(z^{\mathrm{II}}_{i,k}V_{k,j}) - \varepsilon^{\mathrm{II}}_{ij}(\boldsymbol{z})D_{ijkl,m}(\boldsymbol{x})\varepsilon^{\mathrm{II}}_{kl}(\boldsymbol{z})V_m - \sigma^{\mathrm{II}}_{ij}(\boldsymbol{z})\varepsilon^{\mathrm{II}}_{ij}(\boldsymbol{z})\mathrm{div}\,\boldsymbol{V}]\mathrm{d}\Omega. \tag{35}$$

To evaluate all three terms of J^{I} and J^{II} in Eqs. (34) and (35), one needs to *prescribe* an appropriate velocity field $\boldsymbol{V}(\boldsymbol{x})$ and *calculate* actual displacement field $\boldsymbol{z}^{(1)}$ for the initial shape of the cracked body. In other words, a single stress analysis employing a suitable numerical method, such as FEM or the mesh-free method, efficiently evaluates J^{I} and J^{II} components of J-Integral. Similar to the J-Integral it can be easily shown that J^{I} and J^{II} are domain/path independent using divergence theorem as follows.

3.2. Domain independence of J^I and J^{II}

First consider the J^{I} component, by defining $\boldsymbol{V}(\boldsymbol{x}) = \{V_1(\boldsymbol{x}), 0\}^{\mathrm{T}}$, with $V_1(\boldsymbol{x})$ having a value of *unity* at the crack tip, *zero* along the boundary of the domain, and arbitrary elsewhere, the Eq. (34) reduces to

$$J^{\mathrm{I}} = \int_{\Omega}\left(\sigma^{\mathrm{I}}_{ij}(\boldsymbol{z})z^{\mathrm{I}}_{i,1} - \frac{1}{2}\sigma^{\mathrm{I}}_{kl}(\boldsymbol{z})\varepsilon^{\mathrm{I}}_{kl}(\boldsymbol{z})\delta_{1j}\right)\frac{\partial V_1}{\partial x_j}\mathrm{d}\Omega - \int_{\Omega}\frac{1}{2}\varepsilon^{\mathrm{I}}_{ij}(\boldsymbol{z})\frac{\partial D_{ijkl}}{\partial x_1}\varepsilon^{\mathrm{I}}_{kl}(\boldsymbol{z})V_1\,\mathrm{d}\Omega, \tag{36}$$

which can be written as

$$J^{\mathrm{I}} = \int_{\Omega}\left(\sigma^{\mathrm{I}}_{ij}(\boldsymbol{z})z^{\mathrm{I}}_{i,1} - \frac{1}{2}\sigma^{\mathrm{I}}_{kl}(\boldsymbol{z})\varepsilon^{\mathrm{I}}_{kl}(\boldsymbol{z})\delta_{1j}\right)\frac{\partial V_1}{\partial x_j}\mathrm{d}\Omega + \int_{\Omega}\left(\sigma^{\mathrm{I}}_{ij,j}(\boldsymbol{z})z^{\mathrm{I}}_{i,1} + \sigma^{\mathrm{I}}_{ij}(\boldsymbol{z})z^{\mathrm{I}}_{i,1j} - \sigma^{\mathrm{I}}_{ij}(\boldsymbol{z})\varepsilon^{\mathrm{I}}_{ij,1}(\boldsymbol{z}) - \frac{1}{2}\varepsilon^{\mathrm{I}}_{ij}(\boldsymbol{z})\frac{\partial D_{ijkl}}{\partial x_1}\varepsilon^{\mathrm{I}}_{kl}(\boldsymbol{z})\right)V_1\,\mathrm{d}\Omega. \tag{37}$$

Applying the divergence theorem to Eq. (37) yields

$$\begin{aligned} J^{\mathrm{I}} = {} & \int_{\Gamma}\left(\sigma^{\mathrm{I}}_{ij}(\boldsymbol{z})z^{\mathrm{I}}_{i,1} - \frac{1}{2}\sigma^{\mathrm{I}}_{kl}(\boldsymbol{z})\varepsilon^{\mathrm{I}}_{kl}(\boldsymbol{z})\delta_{1j}\right)V_1 n_j\,\mathrm{d}\Gamma - \int_{\Omega}\left(\sigma^{\mathrm{I}}_{ij,j}(\boldsymbol{z})z^{\mathrm{I}}_{i,1} + \sigma^{\mathrm{I}}_{ij}(\boldsymbol{z})z^{\mathrm{I}}_{i,1j} - \sigma^{\mathrm{I}}_{ij}(\boldsymbol{z})\varepsilon^{\mathrm{I}}_{ij,1}(\boldsymbol{z}) - \frac{1}{2}\varepsilon^{\mathrm{I}}_{ij}(\boldsymbol{z})\frac{\partial D_{ijkl}}{\partial x_1}\varepsilon^{\mathrm{I}}_{kl}(\boldsymbol{z})\right)V_1\,\mathrm{d}\Omega \\ & + \int_{\Omega}\left(\sigma^{\mathrm{I}}_{ij,j}(\boldsymbol{z})z^{\mathrm{I}}_{i,1} + \sigma^{\mathrm{I}}_{ij}(\boldsymbol{z})z^{\mathrm{I}}_{i,1j} - \sigma^{\mathrm{I}}_{ij}(\boldsymbol{z})\varepsilon^{\mathrm{I}}_{ij,1}(\boldsymbol{z}) - \frac{1}{2}\varepsilon^{\mathrm{I}}_{ij}(\boldsymbol{z})\frac{\partial D_{ijkl}}{\partial x_1}\varepsilon^{\mathrm{I}}_{kl}(\boldsymbol{z})\right)V_1\,\mathrm{d}\Omega. \end{aligned} \tag{38}$$

and noting that V_1 takes the place of a *weight function* we obtain

$$J^{\mathrm{I}} = \int_{\Gamma}\left(\sigma^{\mathrm{I}}_{ij}(\boldsymbol{z})z^{\mathrm{I}}_{i,1} - \frac{1}{2}\sigma^{\mathrm{I}}_{kl}(\boldsymbol{z})\varepsilon^{\mathrm{I}}_{kl}(\boldsymbol{z})\delta_{1j}\right)n_j\,\mathrm{d}\Gamma, \tag{39}$$

with Γ being the contour surrounding the domain Ω. Once again applying the divergence theorem to Eq. (39) leads to $J^{\mathrm{I}} = 0$ for any closed contour Γ. Hence the J^{I} component is domain/path independent. Similarly the J^{II} component can be shown to be domain/path independent.

3.3. Evaluation of stress-intensity factors

3.3.1. Isotropic functionally graded materials

The mode I and mode II components of J-integral, J^{I} and J^{II} which are also equal to the energy release rates of mode I and mode II, are related to the SIFs K_{I} and K_{II} [25] by the relationships

$$J^{\mathrm{I}} = \frac{K^2_{\mathrm{I}}}{E^*_{\mathrm{tip}}} \tag{40}$$

and

$$J^{\mathrm{II}} = \frac{K^2_{\mathrm{II}}}{E^*_{\mathrm{tip}}}, \tag{41}$$

where E^*_{tip} is equal to E^* evaluated at the crack tip, with E^* being equal to E under plane stress condition and equal to $E/[1-\nu^2]$ under plane strain condition, respectively. From Eqs. (34) and (35) the SIFs K_{I} and K_{II} can be obtained as follows:

$$K_{\mathrm{I}} = \sqrt{J^{\mathrm{I}}E^*_{\mathrm{tip}}} \tag{42}$$

and

$$K_{\mathrm{II}} = \sqrt{J^{\mathrm{II}} E^*_{\mathrm{tip}}}. \tag{43}$$

3.3.2. Orthotropic functionally graded materials

The mode I and mode II components of J-integral, J^{I} and J^{II} which are also equal to the energy release rates of mode I and mode II, are related to the SIFs K_{I} and K_{II} [26] by the relationships

$$J^{\mathrm{I}} = -\frac{K_{\mathrm{I}}}{2} a_{22} \mathrm{Im}\left[\frac{K_{\mathrm{I}}(\mu_1+\mu_2)+K_{\mathrm{II}}}{\mu_1\mu_2}\right] \tag{44}$$

and

$$J^{\mathrm{II}} = \frac{K_{\mathrm{II}}}{2} a_{11} \mathrm{Im}[K_{\mathrm{II}}(\mu_1+\mu_2)+K_{\mathrm{I}}\mu_1\mu_2], \tag{45}$$

where μ_j are the roots of the equation

$$a_{11}\mu^4 - 2a_{16}\mu^3 + (2a_{12}+a_{66})\mu^2 - 2a_{26}\mu + a_{22} = 0, \tag{46}$$

which are either complex or purely imaginary and occur in conjugate pairs, as $\mu_1, \bar{\mu}_1, \mu_2$, and $\bar{\mu}_2$ [27]. In Eq. (46) the coefficients a_{ij} are compliance coefficients with $a_{ij} = a_{ji}$ relating the deformation and stress fields in the solid by the generalized Hooke's law as follows:

$$\varepsilon_i = \sum_{j=1}^{6} a_{ij}\sigma_j \quad i,j = 1,2,\ldots,6. \tag{47}$$

Eqs. (44) and (45) provide a system of linear algebraic equations that can be solved for SIFs $K_{\mathrm{I}}^{(1)}$ and $K_{\mathrm{II}}^{(1)}$ under various mixed-mode loading conditions.

Therefore, the SIFs K_{I} and K_{II} for isotropic and orthotropic FGMs can be evaluated separately using Eqs. (42)–(45). In general both for isotropic and orthotropic FGMs to evaluate the SIFs K_{I} and K_{II}, a numerical method is required for calculating J_{I} and J_{II}.

4. Numerical implementation

4.1. Finite element method

Consider a finite element discretization of a two-dimensional FGM cracked body involving N number of nodes. Let $\boldsymbol{z}^{\mathrm{I}} = (z_1^{\mathrm{I}}, z_2^{\mathrm{I}})$ and $\boldsymbol{z}^{\mathrm{II}} = (z_1^{\mathrm{II}}, z_2^{\mathrm{II}})$ be the mode I and mode II components of the displacement vector, respectively, at the Jth node. If $\boldsymbol{d}^{\mathrm{I}} = \{\boldsymbol{z}_J^{\mathrm{I}}\} \in \mathbb{R}^{2N}$; $J = 1, N$ and $\boldsymbol{d}^{\mathrm{II}} = \{\boldsymbol{z}_J^{\mathrm{II}}\} \in \mathbb{R}^{2N}$; $J = 1, N$ represent global displacement vectors, the mode I and mode II components of J-integral, J^{I} and J^{II} can be approximated by

$$J^{\mathrm{I}} \cong \frac{1}{2}\boldsymbol{d}^{\mathrm{I}^{\mathrm{T}}} \boldsymbol{K}' \boldsymbol{d}^{\mathrm{I}} \tag{48}$$

and

$$J^{\mathrm{II}} \cong \frac{1}{2}\boldsymbol{d}^{\mathrm{II}^{\mathrm{T}}} \boldsymbol{K}' \boldsymbol{d}^{\mathrm{II}}. \tag{49}$$

where $\boldsymbol{K}' = [\boldsymbol{k}'_{IJ}] \in \mathsf{L}(\mathbb{R}^{2N} \times \mathbb{R}^{2N})$; $I, J = 1, N$ is global stiffness sensitivity matrix with $\boldsymbol{k}'_{IJ} \in \boldsymbol{L}(\mathbb{R}^2 \times \mathbb{R}^2)$ representing element-level (domain Ω_{e}) sensitivity matrix, given by

$$\boldsymbol{k}'_{IJ} = \int_{\Omega_{\mathrm{e}}} (\boldsymbol{B}_I^{\mathrm{T}} \boldsymbol{D}(\boldsymbol{x}) \boldsymbol{B}'_J + \boldsymbol{B}_I^{\mathrm{T}} \boldsymbol{D}(\boldsymbol{x}) \boldsymbol{B}'_J - \boldsymbol{B}_I^{\mathrm{T}} \boldsymbol{D}'(\boldsymbol{x}) \boldsymbol{B}_J - \boldsymbol{B}_I^{\mathrm{T}} \boldsymbol{D}(\boldsymbol{x}) \boldsymbol{B}_J \operatorname{div} \boldsymbol{V})\, \mathrm{d}\Omega_{\mathrm{e}}. \tag{50}$$

In Eq. (50),

$$\boldsymbol{D}'(\boldsymbol{x}) = \frac{\partial \boldsymbol{D}(\boldsymbol{x})}{\partial x_1} V_1(\boldsymbol{x}) + \frac{\partial \boldsymbol{D}(\boldsymbol{x})}{\partial x_2} V_2(\boldsymbol{x}), \tag{51}$$

with $\boldsymbol{D}(\boldsymbol{x})$ being the constitutive tensor,

$$\boldsymbol{B}_I(\boldsymbol{x}) = \begin{bmatrix} \Phi_{I,1}(\boldsymbol{x}) & 0 \\ 0 & \Phi_{I,2}(\boldsymbol{x}) \\ \Phi_{I,2}(\boldsymbol{x}) & \Phi_{I,1}(\boldsymbol{x}) \end{bmatrix} \tag{52}$$

and

$$\boldsymbol{B}'_I = \begin{bmatrix} \Phi_{I,1}(\boldsymbol{x})V_{1,1}(\boldsymbol{x}) + \Phi_{I,2}(\boldsymbol{x})V_{2,1}(\boldsymbol{x}) & 0 \\ 0 & \Phi_{I,1}(\boldsymbol{x})V_{1,2}(\boldsymbol{x}) + \Phi_{I,2}(\boldsymbol{x})V_{2,2}(\boldsymbol{x}) \\ \Phi_{I,1}(\boldsymbol{x})V_{1,2}(\boldsymbol{x}) + \Phi_{I,2}(\boldsymbol{x})V_{2,2}(\boldsymbol{x}) & \Phi_{I,1}(\boldsymbol{x})V_{1,1}(\boldsymbol{x}) + \Phi_{I,2}(\boldsymbol{x})V_{2,1}(\boldsymbol{x}) \end{bmatrix}, \tag{53}$$

with $\Phi_{I,i}(\boldsymbol{x})$ serving as the partial derivatives of the shape function corresponding to the Ith node in the ith direction. Eqs. (48) and (49) can be viewed as a discrete analog of the continuum formulation in Eqs. (34) and (35). The former involves simple matrix algebra and, as a result, provides a convenient means for calculating J^{I} and J^{II}.

4.2. Velocity field

The definition of the velocity field is an important step in continuum shape sensitivity analysis. Applying an inappropriate velocity field for shape sensitivity analysis will yield inaccurate sensitivity results. The velocity field must meet numerous, stringent theoretical and practical criteria [28]. Theoretically, (1) the design velocity field must have the same regularity as the displacement field, and (2) depend linearly on the variation of shape design parameters. For two- and three-dimensional elastic solid problems C^0 design velocity fields with integrable first derivatives are required. The regularity requirement comes from the mathematical regularity of design velocity in the design sensitivity expression in Eq. (11). This requirement can also be met by using the displacement shape functions of the finite element analysis to represent design velocity fields. For practical applications, (1) the design velocity computation method must retain the topology of the original finite element mesh, (2) provide finite element boundary nodes that stay on the geometric boundary for all shape changes, (3) use a mathematical rule that guarantees linear dependency of finite element node movements on the variations of shape design parameters, (4) produce a finite element mesh that is not distorted, (5) be naturally linked to design parameters defined on a computer simulation model, (6) allow the mathematical rule to be reusable, and (7) be efficient and general for a large class of applications. A number of methods have been proposed in the literature to compute the velocity field [28]. For a fracture problem, the velocity field $\boldsymbol{V}(\boldsymbol{x})$ is defined with a compact support Ω_c, i.e., $\boldsymbol{V}(\boldsymbol{x})$, is non-*zero* when $\boldsymbol{x} \in \Omega_c$ and is *zero* when $\boldsymbol{x} \in \Omega - \Omega_c$. Hence, the domain Ω in various integrals (see Eqs. (34) and (35)) can be replaced by the sub domain Ω_c. Specifically, consider a rosette of eight 6-noded quarter-point elements around a crack tip, as shown in Fig. 3. These quarter-point elements are standard finite elements commonly employed for fracture analysis of linear-elastic bodies. Assume that the size of these elements is small enough that the rosette can be defined as support Ω_c. Inside Ω_c, the velocity field satisfies the following conditions: (1) the crack tip is assigned a velocity of unit magnitude, i.e., $\boldsymbol{V}(\boldsymbol{0}) = (1/\sqrt{V_{1,\mathrm{tip}}^2 + V_{2,\mathrm{tip}}^2})\{V_{1,\mathrm{tip}}, V_{2,\mathrm{tip}}\}^{\mathrm{T}}$; (2) the velocity at a point on the boundary Γ_c of the rosette is *zero*; and (3) velocity at any point between boundary Γ_c and the crack tip varies linearly. For example, the velocity $\boldsymbol{V}(\boldsymbol{x}_i)$ at the ith node of the quarter-point elements in Fig. 3 can be defined as

$$\boldsymbol{V}(\boldsymbol{x}_i) = \begin{cases} \boldsymbol{0}, & \text{if } i \text{ is a node on the outer ring (open circles),} \\ 0.75\boldsymbol{V}(\boldsymbol{0}), & \text{if } i \text{ is a quarter-point node (closed circles),} \\ \boldsymbol{V}(\boldsymbol{0}), & \text{if } i \text{ is the crack-tip node (closed circle).} \end{cases} \tag{54}$$

Since the velocity field is *zero* on and outside the outer boundary of the quarter point elements, Eqs. (48) and (49) reduces to

$$J^{\mathrm{I}} \cong \frac{1}{2}\sum_{J,K=1}^{M} \boldsymbol{z}_J^{\mathrm{I}^{\mathrm{T}}} \boldsymbol{K}'_{JK} \boldsymbol{z}_K^{\mathrm{I}} \tag{55}$$

and

$$J^{\mathrm{II}} \cong \frac{1}{2}\sum_{J,K=1}^{M} \boldsymbol{z}_J^{\mathrm{II}^{\mathrm{T}}} \boldsymbol{K}'_{JK} \boldsymbol{z}_K^{\mathrm{II}}, \tag{56}$$

where M is the total number of quarter-point and crack-tip nodes in a rosette of focused quarter-point elements near the crack tip, as shown by the closed circles in Fig. 3. In other words, displacement response is only required at an M number of nodes. Since $M \ll N$, the effort in computing J^{I} and J^{II} using Eqs. (55) and (56) is trivial compared to that required for a complete stress analysis.

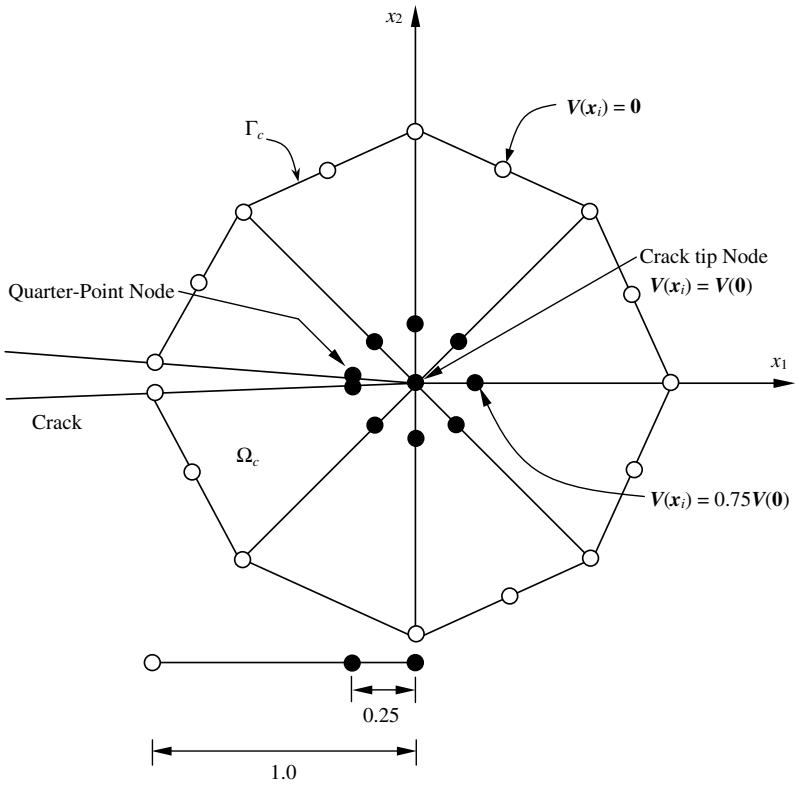

Fig. 3. Rosette of focused quarter-point 6-noded triangular elements near the crack tip.

Compared with existing methods, the proposed method has several advantages: (1) the calculation of SIFs is simple and straightforward as it only requires multiplication of displacement vectors and stiffness sensitivity matrices; (2) since Ω_c is small and the velocity field outside Ω_c is zero, the method only requires displacement response in Ω_c, rendering it computationally efficient; (3) the accuracy of SIF estimates is not affected by a lack of smooth transition between mesh resolutions inside and outside Ω_c, as demonstrated by numerical results; and (4) the method is applicable to multiple interacting cracks even if crack tips are close to one other.

Unlike in the displacement correlation method, and the modified crack-closure integral method SIFs are calculated in the proposed method using displacement response around the crack tip in an average sense. When compared with existing integral based methods such as the J-integral, the J_k^*-integral, and the interaction integral the proposed method requires displacement response only in a small portion around the crack tip. In addition, in case of multiple interacting cracks with crack tips very close to one other, it is very difficult to choose a domain around the crack tip with size enough for accurate evaluation of SIFs using existing integral based methods and hence, the proposed method provides an alternative in such cases. Also, in contrast to existing methods, such as the J_k^*-integral method, there is no need to perform integration along the crack face of the discontinuity (e.g., in calculating J_2^*). Hence, the proposed method is also simpler and more efficient than existing methods.

5. Numerical examples

In conjunction with the newly developed mode decoupling shape sensitivity method, standard FEM was applied to evaluate the SIFs of rectilinear cracks in two-dimensional isotropic and orthotropic FGM structures. Six numerical examples involving mixed-mode (modes I and II) conditions were considered. In all six examples, the elastic modulus varies spatially, while the Poisson's ratio is held constant. This is a reasonable assumption, since variation of the Poisson's ratio is usually small compared with that of the elastic modulus. For numerical integration, a 2×2 Gauss quadrature rule was used in all examples.

The first four numerical examples involve isotropic FGM whereas fifth and sixth numerical examples involve orthotropic FGM structures. The results of orthotropic FGMs obtained in the current study were compared with the semi-analytical solutions of Ozturk and Erdogan [29]. For comparative purposes, the independent orthotropic engineering constants, E_{11}, E_{22}, G_{12}, v_{12}, and v_{21} have been replaced by stiffness parameter E, a stiffness ratio δ^4, an average Poisson's ratio v, and a shear parameter κ [29], which are defined as

$$E = \sqrt{E_{11}E_{22}}, \quad \delta^4 = \frac{E_{11}}{E_{22}} = \frac{v_{12}}{v_{21}}, \quad v = \sqrt{v_{12}v_{21}}, \quad \kappa = \frac{E}{2G_{12}} - v \tag{57}$$

for plane stress, and

$$E = \sqrt{\frac{E_{11}E_{22}}{(1-v_{13}v_{31})(1-v_{23}v_{32})}}, \quad \delta^4 = \frac{E_{11}}{E_{22}}\frac{(1-v_{23}v_{32})}{(1-v_{13}v_{31})}, \quad v = \sqrt{\frac{(v_{12}+v_{13}v_{32})(v_{21}+v_{23}v_{31})}{(1-v_{13}v_{31})(1-v_{23}v_{32})}}, \quad \kappa = \frac{E}{2G_{12}} - v \tag{58}$$

for plane strain.

5.1. Example 1: Edge-cracked plate under mixed-mode loading

This mixed-mode example involves the edge-cracked plate in Fig. 4(a), which is fixed at the bottom and subjected to a far-field shear stress $\tau^{\infty} = 1$ unit applied on the top. The plate has length $L = 16$ units, width $W = 7$ units, and crack length $a = 3.5$ units. The elastic modulus was assumed to follow an exponential function, given by

$$E(x_1) = E_1 \exp\left(\frac{\eta x_1}{W}\right), \quad 0 \leqslant x_1 \leqslant W, \tag{59}$$

where $E_1 = E(0)$, $E_2 = E(W)$, and $\eta = \ln(E_2/E_1)$. In Eq. (59), E_1 and η are two independent material parameters that characterize the elastic modulus variation. The following numerical values were used: $E_1 = 1$ unit, $E_2/E_1 = \exp(\eta) = 0.1$, 0.2, 5, and 10, and $a/W = 0.2$, 0.3, 0.4, 0.5 and 0.6. The Poisson's ratio was held constant with $v = 0.3$. A plane strain condition was assumed. Fig. 4(b) shows FEM discretization involving 2711 nodes, 832 8-noded quadrilateral elements, and 48 focused quarter-point 6-noded triangular elements, adopted to solve with the proposed method. A velocity field $\{V_{1,\text{tip}}, V_{2,\text{tip}}\}^{\mathrm{T}} = \{10^{-5}a, 0\}^{\mathrm{T}}$ was used in the analysis.

Recently, Rao and Rahman [7] also solved this problem using two interaction integrals, referred to as Method-I and Method-II. However, the auxiliary fields employed in Ref. [4] are different from the one defined in the present study. It would be interesting to compare the results of the present method with those of Methods-I and II [7]. Table 1 shows the predicted mixed-mode SIFs for this edge-cracked problem, obtained in the present study for various values of E_2/E_1 using the proposed method. Table 1 also shows the predicted mixed-mode SIFs, obtained for various values of E_2/E_1 using Method-I and Method-II [7]. The results in Table 1 demonstrate that the present method using continuum shape sensitivity provides accurate estimates of K_{I} and K_{II} as compared with corresponding results obtained using previously developed methods.

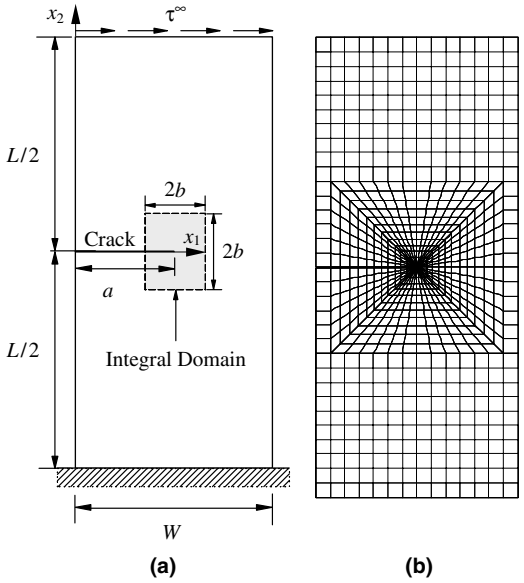

Fig. 4. Edge-cracked plate under mixed-mode loading: (a) geometry, loads, and domain size and (b) FEM discretization.

Table 1
Stress-intensity factors for an edge cracked plate under shear loading

E_2/E_1	Present method		Method-I [7]		Method-II [7]	
	K_{I}	K_{II}	K_{I}	K_{II}	K_{I}	K_{II}
0.1	48.8562	6.1731	48.8532	6.1650	48.8376	6.1714
0.2	43.8421	5.6661	43.8357	5.6606	43.8260	5.6646
1	34.0740	4.5910	34.0624	4.5898	34.0624	4.5898
5	26.3924	3.6361	26.3785	3.6372	26.3839	3.6352
10	23.5780	3.2518	23.5638	3.2532	23.5705	3.2509

5.2. Example 2: Slanted crack in a plate under mixed-mode

Consider a slanted crack in a finite two-dimensional plate with length $L = 2$ units, width $W = 1$ unit and a 45-degree edge crack of normalized length $a/W = 0.4\sqrt{2}$, as shown in Fig. 5(a). The elastic modulus was assumed to follow an exponential function, given by

$$E(x_1) = \overline{E}\exp\left[\eta\left(x_1 - \frac{1}{2}\right)\right], \quad 0 \leqslant x_1 \leqslant W, \tag{60}$$

where $\overline{E}$ and η are two material parameters. For numerical values, $\overline{E} = 1$ unit and $\eta = 0, 0.1, 0.25, 0.5, 0.75$, and 1. The Poisson's ratio was held constant with $\nu = 0.3$. A plane stress condition was assumed. The applied load was prescribed along the upper edge with normal stress $\sigma_{22}(x_1, 1) = \bar{\varepsilon}\overline{E}\exp[\eta(x_1 - 0.5)]$, where $\bar{\varepsilon} = 1$. The displacement boundary condition was specified such that $u_2 = 0$ along the lower edge and, in addition, $u_1 = 0$ for the node on the right side of the lower edge. FEM discretization involved 1541 nodes, 460 8-noded quadrilateral elements, and 40 focused quarter-point 6-noded triangular elements, as shown in Fig. 5(b). A crack-tip velocity $\{V_{1,\mathrm{tip}}, V_{2,\mathrm{tip}}\}^{\mathrm{T}} = \{10^{-5}a\cos\gamma, 10^{-5}a\sin\gamma\}^{\mathrm{T}}$ was used in the analysis. Using the same FEM discretization, the current example was also solved using Methods-I and II by Rao and Rahman [7], as described in the previous example.

Table 2 shows the predicted normalized SIFs $K_{\mathrm{I}}/\bar{\varepsilon}\overline{E}\sqrt{\pi a}$ and $K_{\mathrm{II}}/\bar{\varepsilon}\overline{E}\sqrt{\pi a}$, obtained in the present study for several values of η using the proposed method. Table 2 also shows the predicted normalized SIFs obtained by using Methods-I and II [7] as well as Kim and Paulino's [30] results for various values of η. The results in Table 2 demonstrate that the present method using continuum shape sensitivity provides accurate estimates of K_{I} and K_{II} as compared with the corresponding results of Rao and Rahman [7] and Kim and Paulino [30]. Agreement between the proposed method and reference solutions is excellent.

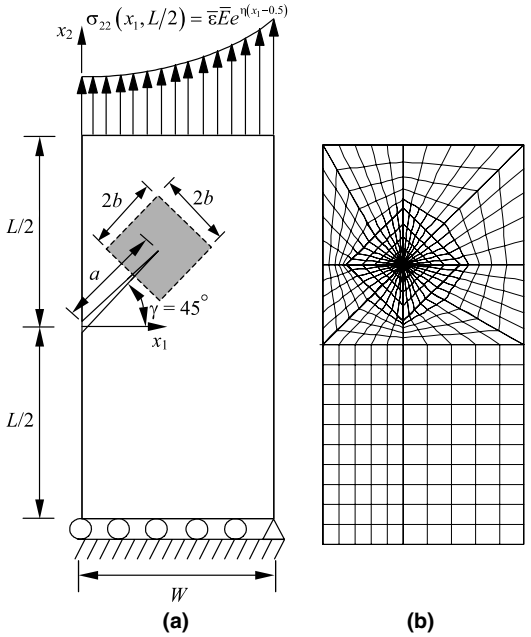

Fig. 5. Slanted crack in a plate under mixed mode loading: (a) geometry and loads and (b) FEM discretization.

Table 2
Normalized stress-intensity factors for a slanted crack in a plate

η	Present method		Method-I [7]		Method-II [7]		Kim and Paulino [30] (J_k^*)	
	$\frac{K_I}{\bar{\varepsilon}\bar{E}\sqrt{\pi a}}$	$\frac{K_{II}}{\bar{\varepsilon}\bar{E}\sqrt{\pi a}}$	$\frac{K_I}{\bar{\varepsilon}\bar{E}\sqrt{\pi a}}$	$\frac{K_{II}}{\bar{\varepsilon}\bar{E}\sqrt{\pi a}}$	$\frac{K_I}{\bar{\varepsilon}\bar{E}\sqrt{\pi a}}$	$\frac{K_{II}}{\bar{\varepsilon}\bar{E}\sqrt{\pi a}}$	$\frac{K_I}{\bar{\varepsilon}\bar{E}\sqrt{\pi a}}$	$\frac{K_{II}}{\bar{\varepsilon}\bar{E}\sqrt{\pi a}}$
0	1.452	0.614	1.448	0.610	1.448	0.610	1.451	0.604
0.1	1.396	0.589	1.392	0.585	1.391	0.585	1.396	0.579
0.25	1.317	0.553	1.313	0.549	1.312	0.549	1.316	0.544
0.5	1.196	0.500	1.193	0.495	1.190	0.495	1.196	0.491
0.75	1.089	0.452	1.086	0.447	1.082	0.446	1.089	0.443
1	0.993	0.409	0.990	0.405	0.986	0.404	0.993	0.402

5.3. Example 3: Plate with an interior inclined crack under mixed-mode

Consider a centrally located inclined crack of length $2a = 2$ units and an orientation γ in a finite, two-dimensional square plate of size $2L = 2W = 20$ units, as shown in Fig. 6. Plane stress conditions were assumed with a constant Poisson's ratio of $\nu = 0.3$. The elastic modulus was assumed to be an exponential function, given by

$$E(x_1) = \bar{E}\exp(\eta x_1), \quad -W \leqslant x_1 \leqslant W, \tag{61}$$

where $\bar{E}$ and η are material parameters. The following data were used for the numerical study: $\bar{E} = 1$ unit; $\eta = 0.25$ and 0.5; and $\gamma/\pi = 0$, 0.1, 0.2, 0.3, 0.4, and 0.5. The applied load corresponds to $\sigma_{22}(x_1, 10) = \bar{\varepsilon}\bar{E}\exp(\eta x_1)$, where $\bar{\varepsilon} = 1$. This stress distribution was obtained by applying nodal forces along the top edge of the plate. The displacement boundary condition was prescribed such that $u_2 = 0$ along the lower edge and, in addition, $u_1 = 0$ for the node on the left hand side of the lower edge. This loading results in a uniform strain $\varepsilon_{22}(x_1, x_2) = \bar{\varepsilon}$ in a corresponding uncracked structure. Fig. 7(a)–(f) show 6 FEM discretizations, each involving 2092 nodes, 628 8-noded quadrilateral elements, and 68 focused quarter-point 6-noded triangular elements, adopted for $\gamma/\pi = 0$, 0.1, 0.2, 0.3, 0.4 and 0.5, respectively. In the analysis, a velocity $\{V_{1,\text{tip}}, V_{2,\text{tip}}\}^T = \{10^{-5}a\cos\gamma, -10^{-5}a\sin\gamma\}^T$ was used at the right crack tip, while a velocity $\{V_{1,\text{tip}}, V_{2,\text{tip}}\}^T = \{-10^{-5}a\cos\gamma, 10^{-5}a\sin\gamma\}^T$ was used at the left crack tip.

Konda and Erdogan [31] previously investigated an infinite plate with a similar configuration. Although an FEM model cannot represent the infinite domains addressed in their analysis, as long as the ratios a/W and a/L are kept relatively small (e.g., $a/W = a/L \leqslant 1/10$), the approximation is acceptable. Tables 3 and 4 provide a comparison between the predicted normalized SIFs for both crack tips, $K_I(+a)/\bar{E}\bar{\varepsilon}\sqrt{\pi a}$, $K_I(-a)/\bar{E}\bar{\varepsilon}\sqrt{\pi a}$, $K_{II}(+a)/\bar{E}\bar{\varepsilon}\sqrt{\pi a}$, and $K_{II}(-a)/\bar{E}\bar{\varepsilon}\sqrt{\pi a}$, obtained by the

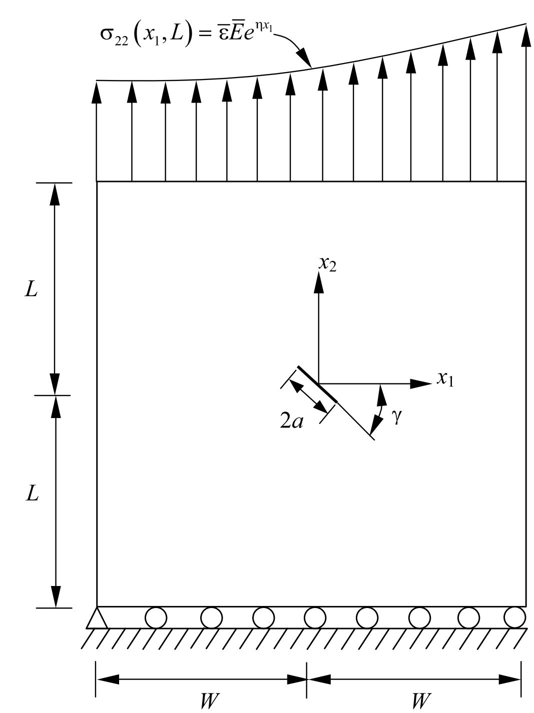

Fig. 6. Plate with an interior inclined crack under mixed mode loading.

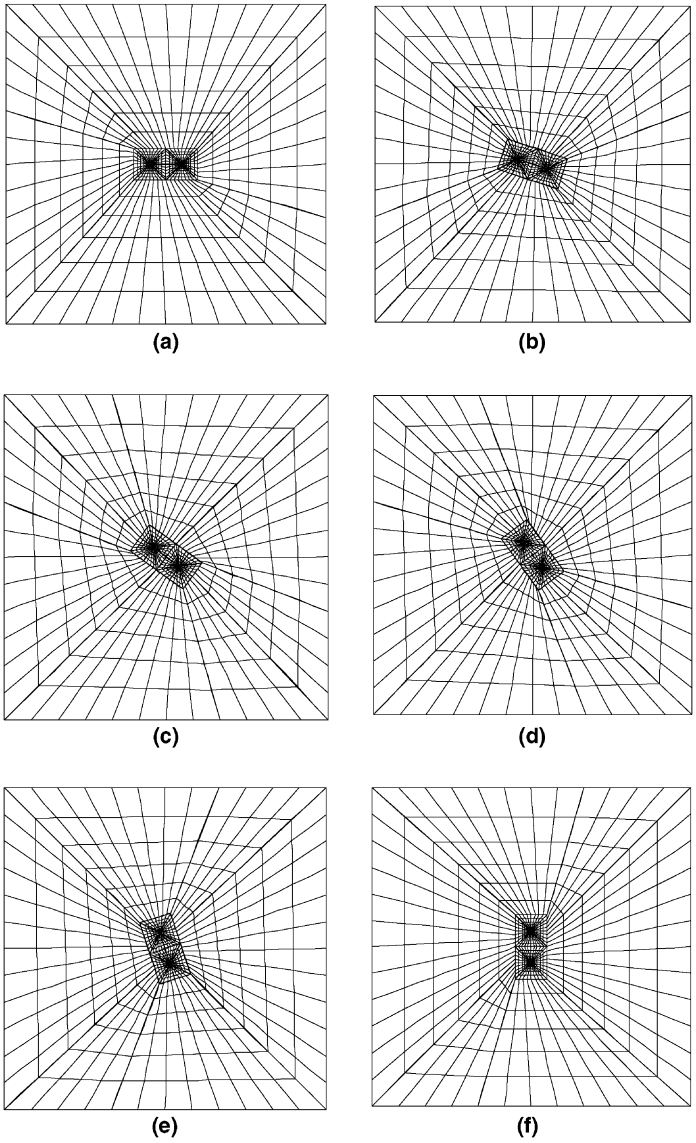

Fig. 7. FEM discretization of plate with an interior inclined crack under mixed mode loading: (a) $\gamma/\pi = 0$; (b) $\gamma/\pi = 0.1$; (c) $\gamma/\pi = 0.2$; (d) $\gamma/\pi = 0.3$; (e) $\gamma/\pi = 0.4$ and (f) $\gamma/\pi = 0.5$.

Table 3
Normalized stress-intensity factors for a plate with an interior inclined crack ($\eta = 0.25$)

Method	γ/π	$\frac{K_I(+a)}{\bar{E}\bar{\varepsilon}\sqrt{\pi a}}$	$\frac{K_I(-a)}{\bar{E}\bar{\varepsilon}\sqrt{\pi a}}$	$\frac{K_{II}(+a)}{\bar{E}\bar{\varepsilon}\sqrt{\pi a}}$	$\frac{K_{II}(-a)}{\bar{E}\bar{\varepsilon}\sqrt{\pi a}}$
Present method	0	1.22471	0.837858	0	0
	0.1	1.10207	0.762755	−0.326716	−0.257921
	0.2	0.790374	0.558607	−0.520307	−0.427262
	0.3	0.415458	0.296924	−0.508223	−0.441699
	0.4	0.117824	0.0808491	−0.304821	−0.283432
	0.5	0	0	0	0
Konda and Erdogan [31]	0	1.196	0.825	0	0
	0.1	1.081	0.750	−0.321	−0.254
	0.2	0.781	0.548	−0.514	−0.422
	0.3	0.414	0.290	−0.504	−0.437
	0.4	0.121	0.075	−0.304	−0.282
	0.5	0	0	0	0

Table 4
Normalized stress-intensity factors for a plate with an interior inclined crack ($\eta = 0.5$)

Method	γ/π	$\frac{K_I(+a)}{\overline{E}\bar{\varepsilon}\sqrt{\pi a}}$	$\frac{K_I(-a)}{\overline{E}\bar{\varepsilon}\sqrt{\pi a}}$	$\frac{K_{II}(+a)}{\overline{E}\bar{\varepsilon}\sqrt{\pi a}}$	$\frac{K_{II}(-a)}{\overline{E}\bar{\varepsilon}\sqrt{\pi a}}$
Present method	0	1.45504	0.676402	0	0
	0.1	1.30674	0.620708	−0.346954	−0.216084
	0.2	0.932016	0.464307	−0.551663	−0.368193
	0.3	0.487678	0.251823	−0.533518	−0.398537
	0.4	0.139743	0.0692727	−0.313425	−0.268601
	0.5	0	0	0	0
Konda and Erdogan [31]	0	1.424	0.674	0	0
	0.1	1.285	0.617	−0.344	−0.213
	0.2	0.925	0.460	−0.548	−0.365
	0.3	0.490	0.247	−0.532	−0.397
	0.4	0.146	0.059	−0.314	−0.269
	0.5	0	0	0	0

proposed method and those of Konda and Erdogan [31] for several values of γ/π, when $\eta = 0.25$ and $\eta = 0.5$, respectively. A good agreement is obtained between present FEM results and Konda and Erdogan's analytical solution.

5.4. Example 4: Plate with two interacting cracks under mixed-mode loading

Consider a finite two-dimensional square plate of size $2L = 2W = 20$ units, containing two cracks of length $2a = 2$ units, oriented with angles $\theta_1 = 30^0$, $\theta_2 = 60^0$, as shown in Fig. 8(a). The distance from the origin to each of the two left crack tips is 1.0 unit. Plane stress conditions were assumed with a constant Poisson's ratio of $v = 0.0$. The elastic modulus was assumed to be an exponential function of x_2, given by

$$E(x_2) = \overline{E}\exp(\beta x_2), \quad -L \leqslant x_2 \leqslant L, \tag{62}$$

where $\overline{E}$ and β are material parameters. The following data were used for the numerical study: $\overline{E} = 1$ unit; and $\beta a = 0.0$, 0.25, 0.5, 0.75, and 1.0. The applied load corresponds to $\sigma_{22}(x_1, \pm 10) = \pm\sigma_0 = 1.0$. This stress distribution was obtained by applying nodal forces along the top edge of the mesh. The displacement boundary condition was prescribed such that $u_2 = 0$ along the lower edge and, in addition, $u_1 = 0$ for the node on the left hand side of the lower edge. FEM discretization involved 3093 nodes, 936 8-noded quadrilateral elements, and 64 focused quarter-point 6-noded triangular elements,

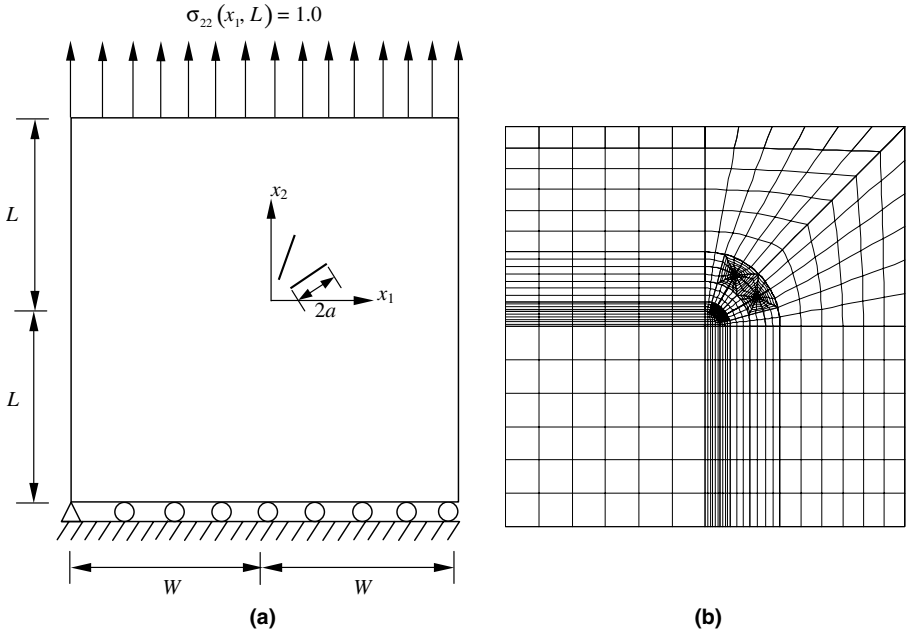

Fig. 8. Plate with two interacting cracks under mixed mode loading: (a) geometry and loads and (b) FEM discretization.

Table 5
Normalized stress-intensity factors for lower crack in multiple interacting cracks

Method	β	$\frac{K_I(-a)}{\sigma_{22}\sqrt{\pi a}}$	$\frac{K_{II}(-a)}{\sigma_{22}\sqrt{\pi a}}$	$\frac{K_I(+a)}{\sigma_{22}\sqrt{\pi a}}$	$\frac{K_{II}(+a)}{\sigma_{22}\sqrt{\pi a}}$
Present method	0.0	0.6005	0.4332	0.8044	0.4200
	0.25	0.6319	0.3938	0.8159	0.4879
	0.5	0.6701	0.3533	0.8418	0.5625
	0.75	0.7076	0.3178	0.8800	0.6450
	1.0	0.7424	0.2867	0.9287	0.7349
Kim and Paulino MCCI [30]	0.0	0.589	0.423	0.804	0.408
	0.25	0.626	0.385	0.816	0.474
	0.5	0.662	0.346	0.842	0.546
	0.75	0.696	0.312	0.880	0.625
	1.0	0.715	0.277	0.930	0.709
Kim and Paulino J_k^*-integral [30]	0.0	0.603	0.431	0.801	0.431
	0.25	0.627	0.401	0.811	0.495
	0.5	0.662	0.363	0.841	0.558
	0.75	0.692	0.347	0.895	0.617
	1.0	0.734	0.298	0.985	0.663
Kim and Paulino DCT [30]	0.0	0.598	0.413	0.812	0.399
	0.25	0.632	0.375	0.818	0.463
	0.5	0.672	0.336	0.838	0.533
	0.75	0.712	0.302	0.869	0.610
	1.0	0.747	0.273	0.910	0.693
Shbeeb et al. [32]	0.0	0.59	0.43	0.78	0.42
	0.25	0.62	0.39	0.82	0.48
	0.5	0.66	0.36	0.88	0.57
	0.75	0.69	0.34	0.98	0.685
	1.0	0.70	0.315	1.10	N/A[a]

[a] Not available.

as shown in Fig. 8(b). Velocities $\{V_{1,\text{tip}}, V_{2,\text{tip}}\}^T = \{10^{-5}a\cos\theta_1, 10^{-5}a\sin\theta_1\}^T$ and $\{V_{1,\text{tip}}, V_{2,\text{tip}}\}^T = \{-10^{-5}a\cos\theta_1, -10^{-5}a\sin\theta_1\}^T$ were employed at right and left crack tips, respectively, of the lower crack.

Kim and Paulino [30] investigated this example using the displacement correlation technique, the modified crack-closure integral method and the J_k^* integral method. In addition, Shbeeb et al. [32] provided semi-analytical solutions obtained using an integral equation method. However, the results of Shbeeb et al. were only presented in graphical form, making accurate verification difficult. Nevertheless, Table 5 provides a comparison between the predicted normalized SIFs, $K_I(+a)/\sigma_{22}\sqrt{\pi a}$, $K_{II}(+a)/\sigma_{22}\sqrt{\pi a}$, $K_I(-a)/\sigma_{22}\sqrt{\pi a}$, and $K_{II}(-a)/\sigma_{22}\sqrt{\pi a}$, for both crack tips of the lower crack obtained

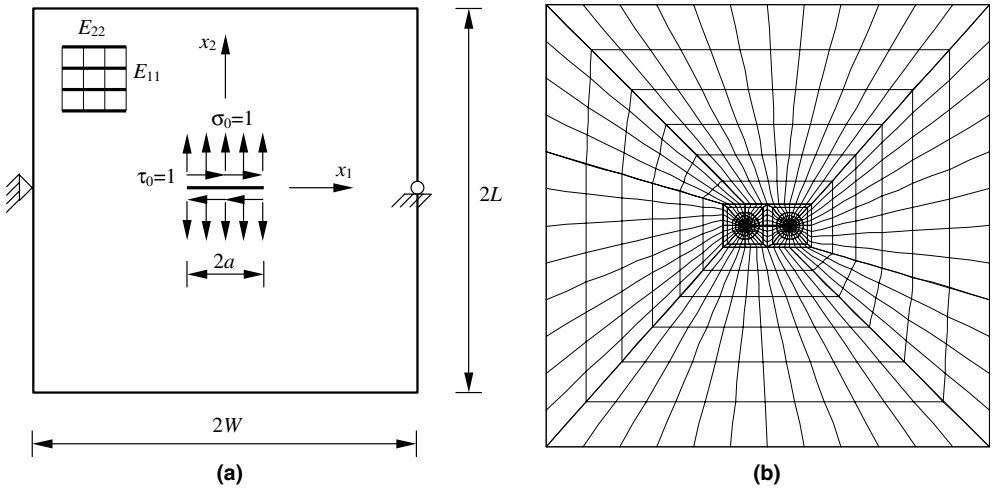

Fig. 9. Plate with an interior crack perpendicular to material gradation: (a) geometry and loads and (b) FEM discretization (2808 nodes, 864 8-noded quadrilateral elements, and 32 focused quarter-point 6-noded triangular elements).

Table 6
The effect of the non-homogeneity parameter on the normalized stress-intensity factors for an orthotropic plate under uniform crack face pressure loading ($\delta^4 = 0.25$, $\nu = 0.3$, $\kappa = 0.5$)

βa	Proposed method		Ozturk and Erdogan [29]	
	$\frac{K_I(a)}{\sigma_0\sqrt{\pi a}}$	$\frac{K_{II}(a)}{\sigma_0\sqrt{\pi a}}$	$\frac{K_I(a)}{\sigma_0\sqrt{\pi a}}$	$\frac{K_{II}(a)}{\sigma_0\sqrt{\pi a}}$
0.0	1.0057	−0.0030	1.0	0.0
0.1	1.0126	0.0220	1.0115	0.0250
0.25	1.0423	0.0629	1.0489	0.0627
0.50	1.1257	0.1285	1.1351	0.1263
1.00	1.3464	0.2640	1.3494	0.2587
2.00	1.8720	0.5643	1.8580	0.5529

Table 7
The effect of the non-homogeneity parameter on the normalized stress-intensity factors for an orthotropic plate under uniform crack face shear loading ($\delta^4 = 0.25$, $\nu = 0.3$, $\kappa = 0.5$)

βa	Proposed method		Ozturk and Erdogan [29]	
	$\frac{K_I(a)}{\tau_0\sqrt{\pi a}}$	$\frac{K_{II}(a)}{\tau_0\sqrt{\pi a}}$	$\frac{K_I(a)}{\tau_0\sqrt{\pi a}}$	$\frac{K_{II}(a)}{\tau_0\sqrt{\pi a}}$
0.0	0.0077	0.9914	0.0	1.0
0.1	−0.0347	0.9905	−0.0494	0.9989
0.25	−0.1085	0.9854	−0.1191	0.9968
0.50	−0.2126	0.9794	−0.2217	0.9965
1.00	−0.3786	0.9898	−0.3862	1.0071
2.00	−0.6203	1.0371	−0.5725	1.0499

Table 8
The effect of the Poisson's ratio on the normalized stress-intensity factors for an orthotropic plate under uniform crack face pressure loading ($\kappa = 5.0$)

βa	$\delta^4 = 0.25$	Proposed method			Ozturk and Erdogan [29]		
	ν	0.15	0.30	0.45	0.15	0.30	0.45
0.5	$K_I(a)/\sigma_0\sqrt{\pi a}$	1.2388	1.2466	1.2543	1.2516	1.2596	1.2674
	$K_{II}(a)/\sigma_0\sqrt{\pi a}$	0.1246	0.1252	0.1258	0.1259	0.1259	0.1259
1.0	$K_I(a)/\sigma_0\sqrt{\pi a}$	1.5552	1.5704	1.5851	1.5589	1.5739	1.5884
	$K_{II}(a)/\sigma_0\sqrt{\pi a}$	0.2587	0.2595	0.2602	0.2555	0.2557	0.2558

Table 9
The effect of the Poisson's ratio on the normalized stress-intensity factors for an orthotropic plate under uniform crack face pressure loading ($\kappa = 5.0$)

βa	$\delta^4 = 10$	Proposed method			Ozturk and Erdogan [29]		
	ν	0.15	0.30	0.45	0.15	0.30	0.45
0.5	$K_I(a)/\sigma_0\sqrt{\pi a}$	1.0601	1.0634	1.0665	1.0748	1.0776	1.0804
	$K_{II}(a)/\sigma_0\sqrt{\pi a}$	0.1204	0.1223	0.1243	0.1252	0.1252	0.1251
1.0	$K_I(a)/\sigma_0\sqrt{\pi a}$	1.1792	1.1861	1.1928	1.1892	1.1955	1.2017
	$K_{II}(a)/\sigma_0\sqrt{\pi a}$	0.2521	0.2541	0.2561	0.2511	0.2512	0.2512

Table 10
The effect of the Poisson's ratio on the normalized stress-intensity factors for an orthotropic plate under uniform crack face shear loading ($\kappa = 5.0$)

βa	$\delta^4 = 0.25$	Proposed method			Ozturk and Erdogan [29]		
	ν	0.15	0.30	0.45	0.15	0.30	0.45
0.5	$K_I(a)/\tau_0\sqrt{\pi a}$	−0.1920	−0.1911	−0.1901	−0.1980	−0.1971	−0.1963
	$K_{II}(a)/\tau_0\sqrt{\pi a}$	0.9607	0.9621	0.9634	0.9898	0.9915	0.9931
1.0	$K_I(a)/\tau_0\sqrt{\pi a}$	−0.3181	−0.3162	−0.3144	−0.3203	−0.3186	−0.3169
	$K_{II}(a)/\tau_0\sqrt{\pi a}$	0.9567	0.9598	0.9627	0.9888	0.9921	0.9953

Table 11
The effect of the Poisson's ratio on the normalized stress-intensity factors for an orthotropic plate under uniform crack face shear loading ($\kappa = 5.0$)

βa	$\delta^4 = 10$	Proposed method			Ozturk and Erdogan [29]		
	v	0.15	0.30	0.45	0.15	0.30	0.45
0.5	$K_I(a)/\tau_0\sqrt{\pi a}$	−0.0328	−0.0328	−0.0328	−0.0366	−0.0365	−0.0365
	$K_{II}(a)/\tau_0\sqrt{\pi a}$	0.9453	0.9453	0.9453	0.9956	0.9961	0.9965
1.0	$K_I(a)/\tau_0\sqrt{\pi a}$	−0.0624	−0.0623	−0.0621	−0.0660	−0.0657	−0.0654
	$K_{II}(a)/\tau_0\sqrt{\pi a}$	0.9397	0.9405	0.9413	0.9913	0.9925	0.9938

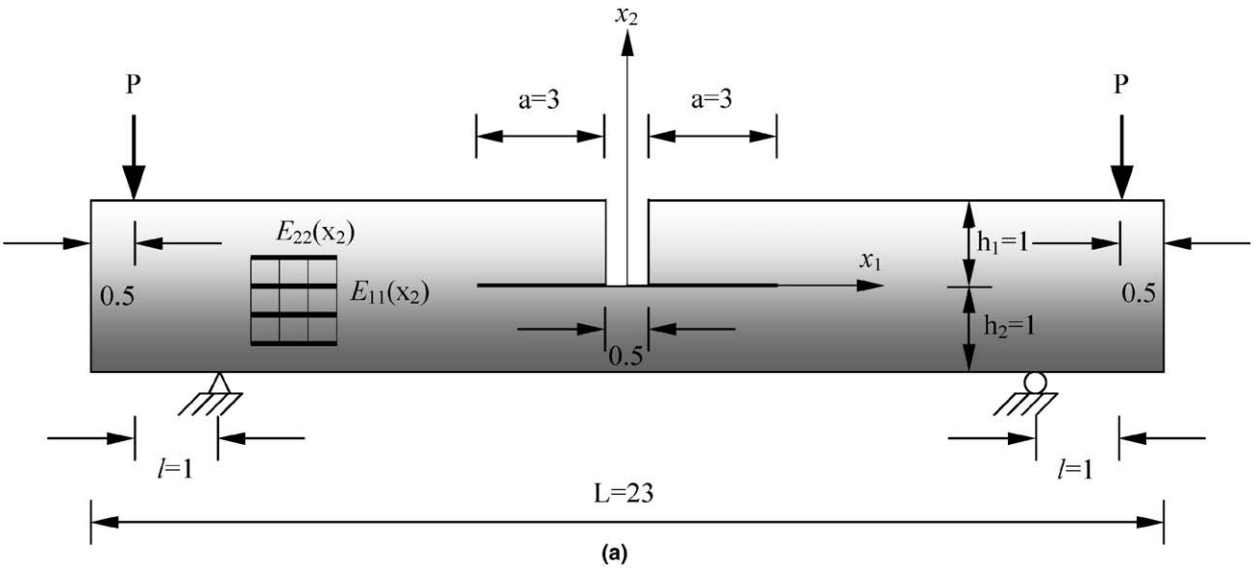

(a)

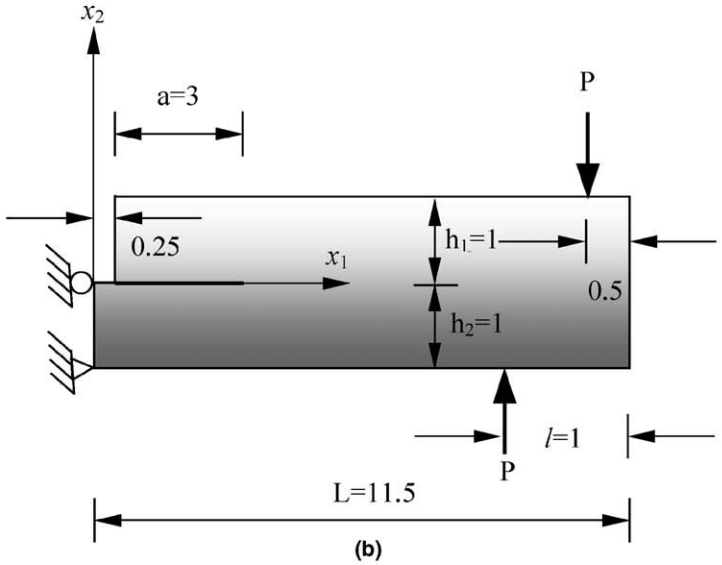

(b)

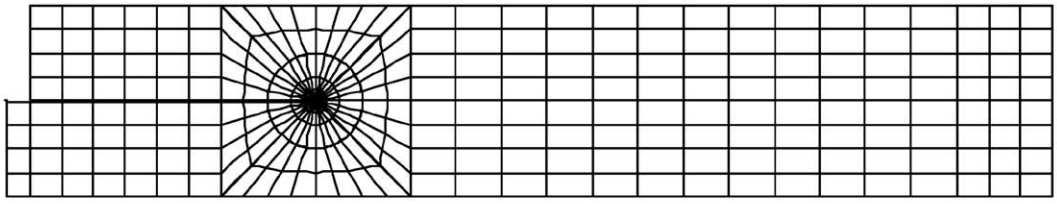

(c)

Fig. 10. Four-point bend specimen under mixed mode loading: (a) geometry and loads, (b) half model and (c) FEM discretization (1357 nodes, 396 8-noded quadrilateral elements, and 32 focused quarter-point 6-noded triangular elements).

by the proposed method and those of Kim and Paulino and Shbeeb et al. for several values of βa. A good agreement is obtained between the present FEM results and published solutions of both Kim and Paulino and Shbeeb et al.

5.5. Example 5: Plate with an interior crack perpendicular to material gradation (mixed mode)

Consider an orthotropic square plate of dimensions $2L = 2W = 20$ units ($L/W = 1$) with a central crack of length $2a = 2.0$ units, as shown in Fig. 9(a). The displacement boundary condition is prescribed, such that $u_1 = u_2 = 0$ for the node in the middle of the left edge, and $u_2 = 0$ for the node in the middle of the right edge. FEM discretization involves 2808 nodes, 864 8-noded quadrilateral elements, and 32 focused quarter-point 6-noded triangular elements in the vicinity of each crack tip, as shown in Fig. 9(b). Both crack-face pressure loading and crack-face shear loading were considered separately. The following material property data were employed for FEM analysis: $E_{11}(x_2) = E^0_{11}e^{\beta x_2}$, $E_{22}(x_2) = E^0_{22}e^{\beta x_2}$, $G_{12}(x_2) = G^0_{12}e^{\beta x_2}$, where the average modulus of elasticity is $E(x_2) = E^0 e^{\beta a(\frac{x_2}{a})}$, with $E^0 = \sqrt{E^0_{11}E^0_{22}}$. The non-homogeneity parameter βa is varied from 0.0 to 2.0. Two different values of the shear parameter$\kappa = 0.5$ and 5.0 and two different stiffness ratios $\delta^4 = 0.25$, and 10 were employed in the FEM analysis. Three different values of the average Poisson's ratio $v = 0.15$,0.30, and 0.45 were used in computations. A plane stress condition and a crack-tip velocity $\{V_{1,\text{tip}}, V_{2,\text{tip}}\}^{\text{T}} = \{10^{-5}a, 0\}^{\text{T}}$ were also assumed.

For crack-face pressure loading the applied load corresponds to $\sigma_{22}(-1 \leqslant x_1 \leqslant 1, \pm 0) = \pm\sigma_0 = \pm 1.0$ and for crack-face shear loading the applied load corresponds to $\sigma_{12}(-1 \leqslant x_1 \leqslant 1, \pm 0) = \pm\tau_0 = \pm 1.0$ along the top and bottom crack faces.

The effect of the non-homogeneity parameter βa and the average Poisson's ratio v on normalized SIFs for both crack-face pressure loading and crack-face shear loading were studied. The results obtained by using the proposed method is compared with those reported by Ozturk and Erdogan [29], who investigated an infinite plate with the same configuration. Tables 6 and 7 provide a comparison between predicted normalized SIFs $K_{\text{I}}(a)/\sigma_0\sqrt{\pi a}$ and $K_{\text{I}}(-a)/\sigma_0\sqrt{\pi a}$ under uniform crack-face pressure loading and uniform crack-face shear loading, respectively, obtained by using the proposed method, and those of Ozturk and Erdogan [29] for various values of non-homogeneity parameter βa, and $\delta^4 = 0.25$; $v = 0.3$; and $\kappa = 0.5$. Tables 8 and 9 provide a comparison between predicted normalized SIFs under uniform crack face pressure loading for $\delta^4 = 0.25$, and $\delta^4 = 10$ respectively, obtained by the proposed method, and those of Ozturk and Erdogan [29] for $v = 0.15$, 0.3, and 0.45 and $\beta a = 0.5$, and 1.0. Tables 10 and 11 provide a similar comparison for an orthotropic plate under uniform crack face shear loading. The agreement between the results of the proposed method and Ozturk and Erdogan's [29] analytical solution is excellent.

5.6. Example 6: Four-point bending specimen under mixed-mode loading

Gu and Asaro [33] investigated the effect of material orthotropy on mixed-mode SIFs in FGMs by considering a four-point bending specimen with exponentially varying Young's moduli, shear modulus, and Poisson's ratio. Fig. 10(a) shows the geometry and boundary conditions of the four-point bending specimen. Due to symmetric geometry and loading with respect to the crack, only a half model of the beam was analyzed, as shown in Fig. 10(b). Fig. 10(c) shows details of FEM mesh discretization for the half beam model involving 1357 nodes, 396 8-noded quadrilateral elements, and 32 focused quarter-point 6-noded triangular elements in the vicinity of the crack tip. Point loads of magnitude P are applied at the nodes $(x_1, x_2) = (10, -1.0)$ and $(x_1, x_2) = (11, 1.0)$. Displacement boundary conditions are prescribed such that $(u_1, u_2) = (0, 0)$ for the node at $(x_1, x_2) = (0, -1.0)$, and $u_1 = 0$ for the node at $(x_1, x_2) = (0, 0)$. Young's moduli, the shear modulus, and Poisson's ratio are exponential functions of x_2 given by: $E_{11}(x_2) = E^0_{11}e^{\beta x_2}$, $E_{22}(x_2) = E^0_{22}e^{\beta x_2}$, $v_{12}(x_2) = v^0_{12}(1 + \varepsilon x_2)e^{\beta x_2}$,

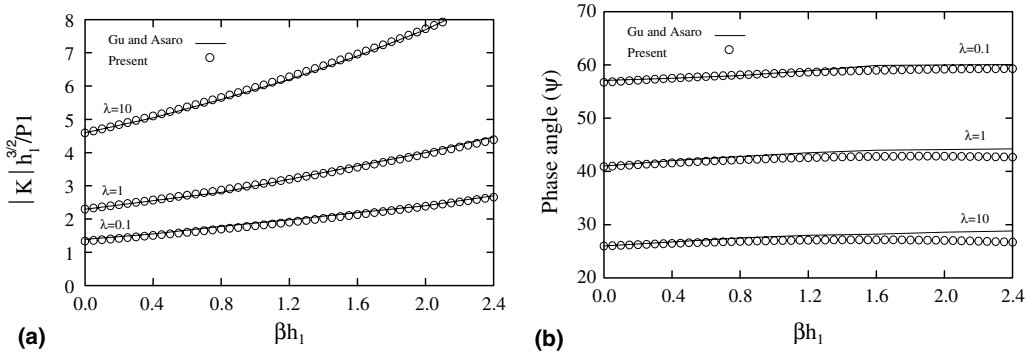

Fig. 11. Four-point bend specimen under mixed mode loading: (a) normalized mixed-mode SIFs $|K|h_1^{3/2}/Pl$ and (b) phase angle $\psi = \tan^{-1}(K_{\text{II}}/K_{\text{I}})$.

$v_{21}(x_2) = v_{21}^0(1+\varepsilon x_2)e^{\beta x_2}$, and $G_{12}(x_2) = E_{22}(x_2)/[2(\sqrt{\lambda}+v_{21}(x_2))]$, where $\lambda = E_{22}(x_2)/E_{11}(x_2)$. Notice that $\lambda = 1/\delta^4$, as explained in Eqs. (57) and (58). The following data were used for the FEM analysis: $a = 3.0$, $h_1/h_2 = 1.0$, $\varepsilon = -0.9$, and $P = 1.0$. A plane stress condition and a crack-tip velocity $\{V_{1,\text{tip}}, V_{2,\text{tip}}\}^{\text{T}} = \{10^{-5}a, 0\}^{\text{T}}$ were also assumed.

Fig. 11(a) and (b) provide a comparison of the SIF $|K|h_1^{3/2}/Pl$ with $|K| = \sqrt{K_{\text{I}}^2 + K_{\text{II}}^2}$, and the phase angle $\psi = \tan^{-1}(K_{\text{II}}/K_{\text{I}})$, respectively, obtained by the proposed method with those values reported by Gu and Asaro [33]. There is quite good agreement between the two solutions, although Gu and Asaro [33] did not provide geometry data. Notice that as βh_1 increases, both the SIF and the phase angle ψ increase, and the material orthotropy (measured by $\lambda = E_{22}/E_{11}$) shows significant influence on the results. Moreover, for a fixed βh_1, as λ increases the SIF increases; however, the phase angle decreases.

6. Summary and conclusions

A new continuum shape sensitivity method was developed for calculating mixed-mode SIFs for a stationary crack in two-dimensional, linear-elastic, FGMs having an arbitrary geometry. The method involves the material derivative concept taken from continuum mechanics, potential energy release rate, and direct differentiation. Compared with existing methods, the proposed method has several advantages: (1) the calculation of SIFs is simple and straightforward as it only requires multiplication of displacement vectors and stiffness sensitivity matrices; (2) since Ω_c is small and the velocity field outside Ω_c is zero, the method only requires displacement response in Ω_c, rendering it computationally efficient; (3) the accuracy of SIF estimates is not affected by a lack of smooth transition between mesh resolutions inside and outside Ω_c, as demonstrated by numerical results; and (4) the method is applicable to multiple interacting cracks even if crack tips are close to one other. An excellent agreement is obtained between the results of the proposed method and previously obtained solutions. Therefore, shape sensitivity analysis provides an attractive alternative for fracture analysis of cracks in homogeneous and non-homogeneous materials.

Acknowledgements

The authors would like to acknowledge the financial support of the US National Science Foundation (NSF) under Award No. CMS 0409463.

References

[1] S. Suresh, A. Mortensen, Fundamentals of Functionally Graded Materials, IOM Communications Ltd., London, 1998.
[2] F. Erdogan, Fracture mechanics of functionally graded materials, Compos. Engrg. 5 (7) (1995) 753–770.
[3] S. Sampath, H. Herman, N. Shimoda, T. Saito, Thermal spray processing of FGMs, MRS Bull. 20 (1) (1995) 27–31.
[4] W.A. Kaysser, B. Ilschner, FGM research activities in Europe, MRS Bull. 20 (1) (1995) 22–26.
[5] H.G. Paulino, Fracture of functionally graded materials, Engrg. Fracture Mech. 69 (14–16) (2002) 1519–1520.
[6] J.H. Kim, H.G. Paulino, Mixed-mode fracture of orthotropic functionally graded materials using finite elements and the modified crack closure method, Engrg. Fracture Mech. 69 (2002) 1557–1586.
[7] B.N. Rao, S. Rahman, Meshfree analysis of cracks in isotropic functionally graded materials, Engrg. Fracture Mech. 70 (2003) 1–27.
[8] B.N. Rao, S. Rahman, An interaction integral method for analysis of cracks in orthotropic functionally graded materials, Comput. Mech. 32 (1–2) (2003) 40–51.
[9] H. Ishikawa, A finite element analysis of stress intensity factors for combined tensile and shear loading by only a virtual crack extension, Int. J. Fracture 16 (1980) R243–R246.
[10] M.E. Gurtin, An Introduction to Continuum Mechanics, Academic Press, New York, NY, 1981.
[11] J. Céa, Problems of shape optimal design, in: E.J. Haug, J. Céa (Eds.), Optimization of Distributed Parameters Structures, Sijthoff and Noordhoff, Alphen a/d Rijn, 1981.
[12] E.J. Haug, K.K. Choi, V. Komkov, Design sensitivity analysis of structural systems, Academic Press, New York, NY, 1986.
[13] J. Fuenmayor, J. Dominguez, E. Giner, J.L. Oliver, Calculation of the stress intensity factor and estimation of its error by a shape sensitivity analysis, Fatigue Fracture Engrg. Mater. Struct. 20 (5) (1997) 813–828.
[14] C.G. Hwang, P.A. Wawrzynek, A.K. Tayebi, A.R. Ingraffea, On the virtual crack extension method for calculation of the rates of energy release rate, Engrg. Fracture Mech. 59 (4) (1998) 521–542.
[15] E. Giner, F.J. Fuenmayor, A.J. Besa, M. Tur, An implementation of the stiffness derivative method as a discrete analytical sensitivity analysis and its application to mixed mode in LEFM, Engrg. Fracture Mech. 69 (18) (2002) 2051–2071.
[16] R.A. Feijóo, C. Padra, R. Saliba, E. Taroco, M.J. Vénere, Shape sensitivity analysis for energy release rate evaluation and its application to the study of three-dimensional cracked bodies, Comput. Methods Appl. Mech. Engrg. 188 (2000) 649–664.
[17] E. Taroco, Shape sensitivity analysis in linear elastic fracture mechanics, Comput. Methods Appl. Mech. Engrg. 188 (2000) 697–712.
[18] T.W. Lee, I.R. Grosse, Energy release rate by a shape design sensitivity approach, Engrg. Fracture Mech. 44 (5) (1993) 807–819.
[19] M. Bonnet, Boundary element based formulations for crack shape sensitivity analysis, Engrg. Anal. Boundary Elements 25 (2001) 347–362.
[20] G. Chen, S. Rahman, Y.H. Park, Shape sensitivity analysis of linear-elastic cracked structures, ASME J. Pressure Vessel Technol. 124 (4) (2002) 476–482.
[21] G. Chen, S. Rahman, Y.H. Park, Shape sensitivity and reliability analyses of linear-elastic cracked structures, Int. J. Fracture 112 (3) (2001) 223–246.

[22] G. Chen, S. Rahman, Y.H. Park, Shape sensitivity analysis in mixed-mode fracture mechanics, Comput. Mech. 27 (4) (2001) 282–291.
[23] B.N. Rao, S. Rahman, A continuum shape sensitivity method for fracture analysis of isotropic functionally graded materials, Comput. Mech. (2006), available online: <http://link.springer-ny.com/link/service/journals/00466/>.
[24] B.N. Rao, S. Rahman, A continuum shape sensitivity method for fracture analysis of orthotropic functionally graded materials, Mech. Mater. 37 (10) (2005) 1007–1025.
[25] J.F. Yau, S.S. Wang, H.T. Corten, A mixed-mode crack analysis of isotropic solids using conservation laws of elasticity, J. Appl. Mech. 47 (1980) 335–341.
[26] S.S. Wang, J.F. Yau, H.T. Corten, A mixed-mode crack analysis of rectilinear anisotropic solids using conservation laws of elasticity, Int. J. Fracture 16 (3) (1980) 247–259.
[27] S.G. Lekhnitskii, S.W. Tsai, T. Cheron, Anisotropic Plates, Gorden and Breach Science Publishers, New York, 1986.
[28] K.K. Choi, K.H. Chang, A study of design velocity field computation for shape optimal design, Finite Elements Anal. Design 15 (1994) 317–341.
[29] M. Oztuk, F. Erdogan, The mixed mode crack problem in an inhomogeneous orthotropic medium, Int. J. Fracture 98 (1999) 243–261.
[30] J.H. Kim, H.G. Paulino, Finite element evaluation of mixed mode stress intensity factors in functionally graded materials, Int. J. Numer. Methods Engrg. 53 (8) (2002) 1903–1935.
[31] N. Konda, F. Erdogan, The mixed mode crack problem in a nonhomogeneous elastic medium, Engrg. Fracture Mech. 47 (4) (1994) 533–545.
[32] N.I. Shbeeb, W.K. Binienda, K.L. Kreider, Analysis of the driving forces for multiple cracks in an infinite nonhomogeneous plate, Part II: Numerical solutions, ASME J. Appl. Mech. 66 (1999) 501–506.
[33] P. Gu, M. Dao, J.R. Asaro, A simplified method for calculating the crack tip field of functionally graded materials using the domain integral, J. Appl. Mech. 66 (1999) 101–108.